

## Behind and Beyond Full-Wave Simulations

Yunchen Yu, Mengqi Xia, Bruce Walter, Eric Michielssen and Steve Marschner

Supplemental Material for ACM TOG paper:

“A Full-Wave Reference Simulator for Computing Surface Reflectance”

This document provides supplemental material for our companion paper, *A Full-Wave Reference Simulator for Computing Surface Reflectance*. With various topics, the document is organized as follows:

- Section 1 contains a more thorough description of the boundary element method (BEM), as compared to the condensed version in the paper.
- Section 2 provides details on the BEM linear system, as well as the approximation schemes underlying the adaptive integral method (AIM), which we use for accelerating matrix computations.
- Section 3 provides derivations of the scattered field quantities in the far field region, as well as strategies we adopted to accelerate our computations of scattered fields.
- Section 4 contains the entire collection of results on our simulated surfaces, as well as a description of the reflection models used for generating these results.

Since these topics are not always closely related, we will refer to sections and equations in our main paper throughout the text, and tie the topics covered in this document to concepts presented in the paper.

## 1 The Boundary Element Method

BEM is a frequency domain method that targets single-wavelength scattering problems, each of which involves incident electric and magnetic fields of a given angular frequency  $\omega$  and a scattering object whose boundary divides the space into two homogeneous regions. The constitutive parameters of the region that contains the incident fields are given by  $(\varepsilon_1, \mu_1)$ , and those of the other region are given by  $(\varepsilon_2, \mu_2)$ . Here,  $\varepsilon_1, \varepsilon_2$  represent the permittivity and  $\mu_1, \mu_2$  represent the permeability.

Notably, in all of our scattering problems, we work with complex-valued field quantities which carry both amplitude and phase information. The field quantities are assumed to be time-harmonic, with their time dependence given by  $e^{j\omega t}$ . For convenience, the term  $e^{j\omega t}$  is suppressed throughout the text. Important symbols involved in BEM are summarized in Table 1.

### 1.1 Maxwell’s Equations and Boundary Conditions

Solving wave scattering problems fundamentally relies on the Maxwell’s equations. The time-harmonic Maxwell’s equations are given by

$$\begin{aligned} \nabla \times \mathbf{E} &= -\mathbf{M} - j\omega\mu\mathbf{H} \\ \nabla \times \mathbf{H} &= \mathbf{J} + j\omega\varepsilon\mathbf{E} \end{aligned} \tag{S.1}$$

where  $\mathbf{E}$  and  $\mathbf{H}$  are the electric and magnetic fields, and  $\mathbf{J}$  and  $\mathbf{M}$  are the time-harmonic electric and magnetic current densities.

$j$	Imaginary unit for complex numbers, i.e. $j^2 = -1$
$\omega$	Angular frequency of light
$\varepsilon$	Permittivity of a homogeneous region
$\mu$	Permeability of a homogeneous region
<b>E</b>	Electric field
<b>H</b>	Magnetic field
<b>J</b>	Electric current density
<b>M</b>	Magnetic current density
<b>n</b>	Normal vector on the object boundary
$\lambda$	Wavelength of the light in vacuum
$\eta$	Refractive index of a particular medium
$k$	Wavenumber of the light in a particular medium
$\mathbf{r}, \mathbf{r}'$	Position of points in the 3D space
$G(\mathbf{r}, \mathbf{r}')$	Green's function

Table 1: List of symbols frequently used in BEM.

Moreover, at the interface between two regions  $R_1$  and  $R_2$  with possibly different constitutive parameters, the generalized electromagnetic boundary conditions can be written as

$$\begin{aligned}\hat{\mathbf{n}} \times (\mathbf{E}_1 - \mathbf{E}_2) &= -\mathbf{M} \\ \hat{\mathbf{n}} \times (\mathbf{H}_1 - \mathbf{H}_2) &= \mathbf{J}\end{aligned}\tag{S.2}$$

where  $\mathbf{n}$  is the normal vector on the interface that points into  $R_1$ .

## 1.2 Two Half-Problems and Fictitious Currents

Many discussions on BEM, for instance, those in [Gibson \(2021\)](#) and [Xia et al. \(2020\)](#), include the step of dividing the scattering problems into two half-problems. In our paper, we did not include discussions on these two half problems and instead provided a high-level description of the method and figure illustrations. In this document, we provide more detailed explanations on the exterior and interior half problems.

As illustrated in Fig. 1, the total fields in the regions  $R_1, R_2$  are denoted by  $(\mathbf{E}_1, \mathbf{H}_1)$  and  $(\mathbf{E}_2, \mathbf{H}_2)$ . In the exterior problem, the constitutive parameters on both sides of the object boundary are set to  $(\varepsilon_1, \mu_1)$ . The fields outside the boundary remain unchanged, while the fields inside the object boundary are set to null fields. Importantly, fictitious currents  $\mathbf{J}_1$  and  $\mathbf{M}_1$  are introduced on the object boundary, in order to support this discontinuity in electromagnetic field values across the object boundary. According to Eq. S.2, the current densities  $\mathbf{J}_1$  and  $\mathbf{M}_1$  satisfy

$$\mathbf{J}_1 = \hat{\mathbf{n}} \times \mathbf{H}_1; \quad \mathbf{M}_1 = -\hat{\mathbf{n}} \times \mathbf{E}_1\tag{S.3}$$

In the interior problem, the constitutive parameters on both sides of the boundary are set to  $(\varepsilon_2, \mu_2)$ . The fields outside the boundary are null fields, while the internal fields  $(\mathbf{E}_2, \mathbf{H}_2)$  remain unchanged. The currents  $\mathbf{J}_2, \mathbf{M}_2$  are similarly introduced, satisfying

$$\mathbf{J}_2 = -\hat{\mathbf{n}} \times \mathbf{H}_2; \quad \mathbf{M}_2 = \hat{\mathbf{n}} \times \mathbf{E}_2\tag{S.4}$$

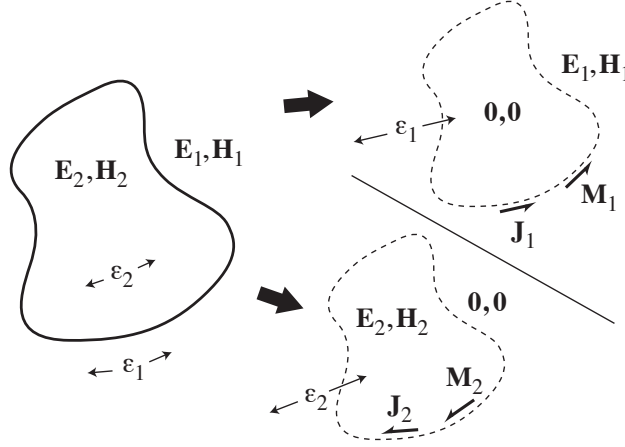


Figure 1: An overview of BEM. The scattering problem is divided into two half problems. This figure was originally presented in [Xia et al. \(2020\)](#).

In both Eq. S.3 and S.4,  $\mathbf{n}$  is the normal vector on the interface between  $R_1$  and  $R_2$  that points into  $R_1$  (introducing the factor of  $-1$  in Eq. S.4 as compared to Eq. S.3).

Moreover, we write the fields in  $R_1$  as the sum of the incident fields  $\mathbf{E}_i, \mathbf{H}_i$  and the scattered fields  $\mathbf{E}_s, \mathbf{H}_s$ , which propagate outward from the scattering object. This gives us:

$$\mathbf{E}_1 = \mathbf{E}_i + \mathbf{E}_s; \quad \mathbf{H}_1 = \mathbf{H}_i + \mathbf{H}_s \quad (\text{S.5})$$

### 1.3 Source-Field Relationships

The fictitious currents  $\mathbf{J}_1, \mathbf{M}_1, \mathbf{J}_2$ , and  $\mathbf{M}_2$  serve two important functions. For one, they support the discontinuities in field values across the object boundary in the aforementioned half-problems. For another, they can be considered the sources that radiate the fields  $(\mathbf{E}_s, \mathbf{H}_s)$  and  $(\mathbf{E}_2, \mathbf{H}_2)$ . Specifically, the fields  $\mathbf{E}_s$  and  $\mathbf{H}_s$  can be seen as generated by the currents  $\mathbf{J}_1, \mathbf{M}_1$ , radiating in a homogeneous medium with constitutive parameters  $(\epsilon_1, \mu_1)$ .  $\mathbf{E}_2$  and  $\mathbf{H}_2$  can be seen as generated by the currents  $\mathbf{J}_2, \mathbf{M}_2$ , radiating in a homogeneous medium with constitutive parameters  $(\epsilon_2, \mu_2)$ . This way, the field quantities can be represented in terms of these introduced surface currents. Therefore, solving a scattering problem becomes simpler, as it is sufficient to solve for the current densities on the lower dimension boundary. The source-field relationships for homogeneous media are derived from Maxwell's equations and are given by

$$\begin{aligned} \mathbf{E}(\mathbf{r}) &= -j\omega\mu(\mathcal{L}\mathbf{J})(\mathbf{r}) - (\mathcal{K}\mathbf{M})(\mathbf{r}) \\ \mathbf{H}(\mathbf{r}) &= -j\omega\epsilon(\mathcal{L}\mathbf{M})(\mathbf{r}) + (\mathcal{K}\mathbf{J})(\mathbf{r}) \end{aligned} \quad (\text{S.6})$$

where

$$\begin{aligned} (\mathcal{L}\mathbf{X})(\mathbf{r}) &= [1 + \frac{1}{k^2}\nabla\nabla\cdot]\int_V G(\mathbf{r}, \mathbf{r}')\mathbf{X}(\mathbf{r}')d\mathbf{r}' \\ (\mathcal{K}\mathbf{X})(\mathbf{r}) &= \nabla \times \int_V G(\mathbf{r}, \mathbf{r}')\mathbf{X}(\mathbf{r}')d\mathbf{r}' \end{aligned} \quad (\text{S.7})$$

Here  $k$  is the wavenumber, given by  $k = 2\pi\eta/\lambda$ , where  $\eta$  is the refractive index of the medium and  $\lambda$  is the source field's wavelength in vacuum.  $G(\mathbf{r}, \mathbf{r}')$  is the 3D Green's function for the scalar Helmholtz equation

$$G(\mathbf{r}, \mathbf{r}') = \frac{e^{-jkr}}{4\pi r} \quad \text{where } r = |\mathbf{r} - \mathbf{r}'|. \quad (\text{S.8})$$

Eq. S.6 can be applied in both half-problems, giving rise to

$$\begin{aligned} \mathbf{E}_s(\mathbf{r}) &= -j\omega\mu_1(\mathcal{L}_1\mathbf{J}_1)(\mathbf{r}) - (\mathcal{K}_1\mathbf{M}_1)(\mathbf{r}) \\ \mathbf{H}_s(\mathbf{r}) &= -j\omega\varepsilon_1(\mathcal{L}_1\mathbf{M}_1)(\mathbf{r}) + (\mathcal{K}_1\mathbf{J}_1)(\mathbf{r}) \end{aligned} \quad (\text{S.9})$$

and

$$\begin{aligned} \mathbf{E}_2(\mathbf{r}) &= -j\omega\mu_2(\mathcal{L}_2\mathbf{J}_2)(\mathbf{r}) - (\mathcal{K}_2\mathbf{M}_2)(\mathbf{r}) \\ \mathbf{H}_2(\mathbf{r}) &= -j\omega\varepsilon_2(\mathcal{L}_2\mathbf{M}_2)(\mathbf{r}) + (\mathcal{K}_2\mathbf{J}_2)(\mathbf{r}) \end{aligned} \quad (\text{S.10})$$

Since the operators  $\mathcal{L}, \mathcal{K}$  assume different forms in different media, we use the subscripts 1 and 2 to distinguish between these forms.

Lastly, in a real, physical scattering problem, the tangential component of the electromagnetic field is always continuous across the object boundary, and according to Eq. S.2, the net current densities on the object boundary should be zero. This means that the fictitious surface currents we introduced need to cancel out from the two sides of the surface, allowing us to write

$$\mathbf{J} = \mathbf{J}_1 = -\mathbf{J}_2; \quad \mathbf{M} = \mathbf{M}_1 = -\mathbf{M}_2 \quad (\text{S.11})$$

## 1.4 Integral Equations

Combining Eq. S.3, S.4, S.5, S.9, S.10, and S.11 gives us

$$\begin{aligned} [j\omega\mu_1(\mathcal{L}_1\mathbf{J})(\mathbf{r}) + j\omega\mu_2(\mathcal{L}_2\mathbf{J})(\mathbf{r}) + (\mathcal{K}_1\mathbf{M})(\mathbf{r}) + (\mathcal{K}_2\mathbf{M})(\mathbf{r})]_{\tan} &= [\mathbf{E}_i]_{\tan} \\ [(\mathcal{K}_1\mathbf{J})(\mathbf{r}) + (\mathcal{K}_2\mathbf{J})(\mathbf{r}) - j\omega\varepsilon_1(\mathcal{L}_1\mathbf{M})(\mathbf{r}) - j\omega\varepsilon_2(\mathcal{L}_2\mathbf{M})(\mathbf{r})]_{\tan} &= -[\mathbf{H}_i]_{\tan} \end{aligned} \quad (\text{S.12})$$

which hold on every point  $\mathbf{r}$  on the surface. Here, the “tan” notation refers to the component of the field that is tangent to surface at each point  $\mathbf{r}$ . As noted in Gibson (2021), these equations are the PMCHWT electric field integral equation (EFIE) and magnetic field integral equation (MFIE). Eq. S.12 is the same as Eq. 10 in our paper, while our formulation of it in this document has included more steps.

With the EFIE and MFIE, one can solve for the fictitious current densities  $\mathbf{J}, \mathbf{M}$  on the surface, and use them to compute the scattered fields from the object with the source-fields relationships. The discussion on these steps can be found in Eq. 11–20 in the paper, as well as the next section of this document.

## 2 Linear System and the Adaptive Integral Method

Eq. 12–18 in the main paper provides a high-level description of the BEM linear system. For 3D scattering problems, evaluating each of the matrix elements in the BEM linear system, not to mention solving the

linear system using some direct solver, is extremely expensive. In practice, the linear system is solved iteratively, with the matrix-vector multiplication step accelerated using AIM. In this section, we expand on the exact form of the BEM linear system, as well as the approximations underlying AIM which accelerate our matrix computations while retaining the high accuracy in our simulations.

## 2.1 Matrix Elements

Expanding Eq. 13–16 in our paper and applying the definitions of the  $\mathcal{L}, \mathcal{K}$  operators in Eq. S.7 (and using some vector calculus identities), we can write the BEM matrix elements as follows:

$$\begin{aligned} A_{\text{EJ}}^{mn} &= j\omega\mu_1 \int_{\mathbf{f}_m} \int_{\mathbf{f}_n} \mathbf{f}_m(\mathbf{r}) \cdot \mathbf{f}_n(\mathbf{r}') G_1(\mathbf{r}, \mathbf{r}') d\mathbf{r}' d\mathbf{r} \\ &\quad - \frac{j}{\omega\varepsilon_1} \int_{\mathbf{f}_m} \int_{\mathbf{f}_n} \nabla \cdot \mathbf{f}_m(\mathbf{r}) G_1(\mathbf{r}, \mathbf{r}') \nabla' \cdot \mathbf{f}_n(\mathbf{r}') d\mathbf{r}' d\mathbf{r} \\ &\quad + j\omega\mu_2 \int_{\mathbf{f}_m} \int_{\mathbf{f}_n} \mathbf{f}_m(\mathbf{r}) \cdot \mathbf{f}_n(\mathbf{r}') G_2(\mathbf{r}, \mathbf{r}') d\mathbf{r}' d\mathbf{r} \\ &\quad - \frac{j}{\omega\varepsilon_2} \int_{\mathbf{f}_m} \int_{\mathbf{f}_n} \nabla \cdot \mathbf{f}_m(\mathbf{r}) G_2(\mathbf{r}, \mathbf{r}') \nabla' \cdot \mathbf{f}_n(\mathbf{r}') d\mathbf{r}' d\mathbf{r} \end{aligned} \quad (\text{S.13})$$

$$\begin{aligned} A_{\text{EM}}^{mn} = A_{\text{HJ}}^{mn} &= \int_{\mathbf{f}_m} \int_{\mathbf{f}_n} \mathbf{f}_m(\mathbf{r}) \cdot [\nabla G_1(\mathbf{r}, \mathbf{r}') \times \mathbf{f}_n(\mathbf{r}')] d\mathbf{r}' d\mathbf{r} \\ &\quad + \int_{\mathbf{f}_m} \int_{\mathbf{f}_n} \mathbf{f}_m(\mathbf{r}) \cdot [\nabla G_2(\mathbf{r}, \mathbf{r}') \times \mathbf{f}_n(\mathbf{r}')] d\mathbf{r}' d\mathbf{r} \end{aligned} \quad (\text{S.14})$$

$$\begin{aligned} A_{\text{HM}}^{mn} &= -j\omega\varepsilon_1 \int_{\mathbf{f}_m} \int_{\mathbf{f}_n} \mathbf{f}_m(\mathbf{r}) \cdot \mathbf{f}_n(\mathbf{r}') G_1(\mathbf{r}, \mathbf{r}') d\mathbf{r}' d\mathbf{r} \\ &\quad + \frac{j}{\omega\mu_1} \int_{\mathbf{f}_m} \int_{\mathbf{f}_n} \nabla \cdot \mathbf{f}_m(\mathbf{r}) G_1(\mathbf{r}, \mathbf{r}') \nabla' \cdot \mathbf{f}_n(\mathbf{r}') d\mathbf{r}' d\mathbf{r} \\ &\quad - j\omega\varepsilon_2 \int_{\mathbf{f}_m} \int_{\mathbf{f}_n} \mathbf{f}_m(\mathbf{r}) \cdot \mathbf{f}_n(\mathbf{r}') G_2(\mathbf{r}, \mathbf{r}') d\mathbf{r}' d\mathbf{r} \\ &\quad + \frac{j}{\omega\mu_2} \int_{\mathbf{f}_m} \int_{\mathbf{f}_n} \nabla \cdot \mathbf{f}_m(\mathbf{r}) G_2(\mathbf{r}, \mathbf{r}') \nabla' \cdot \mathbf{f}_n(\mathbf{r}') d\mathbf{r}' d\mathbf{r} \end{aligned} \quad (\text{S.15})$$

where  $\mathbf{f}_m, \mathbf{f}_n$  refer to basis functions and  $G_1(\mathbf{r}, \mathbf{r}')$  and  $G_2(\mathbf{r}, \mathbf{r}')$  are the 3D Green's functions defined in regions  $R_1, R_2$ . Note that the  $\nabla$  operator takes derivatives with respect to  $\mathbf{r}$  and the  $\nabla'$  operator takes derivatives with respect to  $\mathbf{r}'$ . The above expressions show that each matrix element in  $A_{\text{EJ}}, A_{\text{EM}}, A_{\text{HJ}}, A_{\text{HM}}$  consists of two components of the same form, pertaining to the two homogeneous media involved in the scattering problem. Thus, we can write:

$$A_{\text{X}}^{mn} = A_{\text{X},1}^{mn} + A_{\text{X},2}^{mn} \quad \text{for } \text{X} \in \{\text{EJ}, \text{EM}, \text{HJ}, \text{HM}\} \quad (\text{S.16})$$

We now define some shift-invariant functions for both regions ( $i = 1, 2$ ):

$$\begin{aligned} g_{1,i}(\mathbf{r} - \mathbf{r}') &= G_i(\mathbf{r}, \mathbf{r}') = \frac{e^{-jk_ir}}{4\pi r} \\ g_{2,i}(\mathbf{r} - \mathbf{r}') &= \hat{\mathbf{x}} \cdot \nabla G_i(\mathbf{r}, \mathbf{r}') = -(x - x') \left( \frac{1 + jk_ir}{4\pi r^3} \right) e^{-jk_ir} \\ g_{3,i}(\mathbf{r} - \mathbf{r}') &= \hat{\mathbf{y}} \cdot \nabla G_i(\mathbf{r}, \mathbf{r}') = -(y - y') \left( \frac{1 + jk_ir}{4\pi r^3} \right) e^{-jk_ir} \\ g_{4,i}(\mathbf{r} - \mathbf{r}') &= \hat{\mathbf{z}} \cdot \nabla G_i(\mathbf{r}, \mathbf{r}') = -(z - z') \left( \frac{1 + jk_ir}{4\pi r^3} \right) e^{-jk_ir} \quad \text{where } r = |\mathbf{r} - \mathbf{r}'| \end{aligned} \quad (\text{S.17})$$

Here,  $x, y, z, x', y', z'$  are the Cartesian components of  $\mathbf{r}, \mathbf{r}'$ . Now we have for  $i = 1, 2$ :

$$\begin{aligned} A_{\text{EJ},i}^{mn} &= j\omega\mu_i \int_{\mathbf{f}_m} \int_{\mathbf{f}_n} \mathbf{f}_{mx}(\mathbf{r}) g_{1,i}(\mathbf{r} - \mathbf{r}') \mathbf{f}_{nx}(\mathbf{r}') d\mathbf{r}' d\mathbf{r} \\ &\quad + j\omega\mu_i \int_{\mathbf{f}_m} \int_{\mathbf{f}_n} \mathbf{f}_{my}(\mathbf{r}) g_{1,i}(\mathbf{r} - \mathbf{r}') \mathbf{f}_{ny}(\mathbf{r}') d\mathbf{r}' d\mathbf{r} \\ &\quad + j\omega\mu_i \int_{\mathbf{f}_m} \int_{\mathbf{f}_n} \mathbf{f}_{mz}(\mathbf{r}) g_{1,i}(\mathbf{r} - \mathbf{r}') \mathbf{f}_{nz}(\mathbf{r}') d\mathbf{r}' d\mathbf{r} \\ &\quad - \frac{j}{\omega\varepsilon_i} \int_{\mathbf{f}_m} \int_{\mathbf{f}_n} \nabla \cdot \mathbf{f}_m(\mathbf{r}) g_{1,i}(\mathbf{r} - \mathbf{r}') \nabla' \cdot \mathbf{f}_n(\mathbf{r}') d\mathbf{r}' d\mathbf{r} \end{aligned} \quad (\text{S.18})$$

where  $\mathbf{f}_{mx}, \mathbf{f}_{my}, \mathbf{f}_{mz}$  are the  $x, y, z$  components of the vector basis function  $\mathbf{f}_m$ . Similarly, we have:

$$\begin{aligned} A_{\text{EM},i}^{mn} = A_{\text{HJ},i}^{mn} &= \int_{\mathbf{f}_m} \int_{\mathbf{f}_n} \mathbf{f}_{mz}(\mathbf{r}) g_{2,i}(\mathbf{r} - \mathbf{r}') \mathbf{f}_{ny}(\mathbf{r}') d\mathbf{r}' d\mathbf{r} \\ &\quad - \int_{\mathbf{f}_m} \int_{\mathbf{f}_n} \mathbf{f}_{my}(\mathbf{r}) g_{2,i}(\mathbf{r} - \mathbf{r}') \mathbf{f}_{nz}(\mathbf{r}') d\mathbf{r}' d\mathbf{r} \\ &\quad + \int_{\mathbf{f}_m} \int_{\mathbf{f}_n} \mathbf{f}_{mx}(\mathbf{r}) g_{3,i}(\mathbf{r} - \mathbf{r}') \mathbf{f}_{nz}(\mathbf{r}') d\mathbf{r}' d\mathbf{r} \\ &\quad - \int_{\mathbf{f}_m} \int_{\mathbf{f}_n} \mathbf{f}_{mz}(\mathbf{r}) g_{3,i}(\mathbf{r} - \mathbf{r}') \mathbf{f}_{nx}(\mathbf{r}') d\mathbf{r}' d\mathbf{r} \\ &\quad + \int_{\mathbf{f}_m} \int_{\mathbf{f}_n} \mathbf{f}_{my}(\mathbf{r}) g_{4,i}(\mathbf{r} - \mathbf{r}') \mathbf{f}_{nx}(\mathbf{r}') d\mathbf{r}' d\mathbf{r} \\ &\quad - \int_{\mathbf{f}_m} \int_{\mathbf{f}_n} \mathbf{f}_{mx}(\mathbf{r}) g_{4,i}(\mathbf{r} - \mathbf{r}') \mathbf{f}_{ny}(\mathbf{r}') d\mathbf{r}' d\mathbf{r} \end{aligned} \quad (\text{S.19})$$

Lastly, we also have:

$$\begin{aligned} A_{\text{HM},i}^{mn} &= -j\omega\varepsilon_i \int_{\mathbf{f}_m} \int_{\mathbf{f}_n} \mathbf{f}_{mx}(\mathbf{r}) g_{1,i}(\mathbf{r} - \mathbf{r}') \mathbf{f}_{nx}(\mathbf{r}') d\mathbf{r}' d\mathbf{r} \\ &\quad - j\omega\varepsilon_i \int_{\mathbf{f}_m} \int_{\mathbf{f}_n} \mathbf{f}_{my}(\mathbf{r}) g_{1,i}(\mathbf{r} - \mathbf{r}') \mathbf{f}_{ny}(\mathbf{r}') d\mathbf{r}' d\mathbf{r} \\ &\quad - j\omega\varepsilon_i \int_{\mathbf{f}_m} \int_{\mathbf{f}_n} \mathbf{f}_{mz}(\mathbf{r}) g_{1,i}(\mathbf{r} - \mathbf{r}') \mathbf{f}_{nz}(\mathbf{r}') d\mathbf{r}' d\mathbf{r} \\ &\quad + \frac{j}{\omega\mu_i} \int_{\mathbf{f}_m} \int_{\mathbf{f}_n} \nabla \cdot \mathbf{f}_m(\mathbf{r}) g_{1,i}(\mathbf{r} - \mathbf{r}') \nabla' \cdot \mathbf{f}_n(\mathbf{r}') d\mathbf{r}' d\mathbf{r} \end{aligned} \quad (\text{S.20})$$

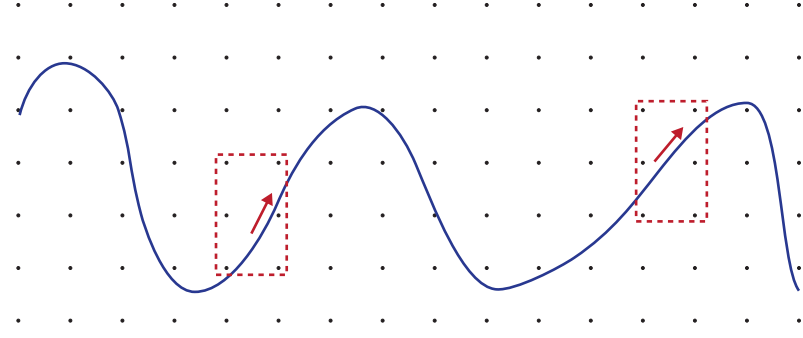


Figure 2: A Cartesian grid surrounding the surface sample, illustrated in 2D. The red boxes indicate that each basis function can be approximated by a collection of nearby point sources. The Cartesian grid and point source approximation are established in 3D in our simulations.

Eq. S.18, S.19, and S.20 reveal that each element in each of the four blocks in the BEM matrix can be written as the linear combination of a few terms in the form of

$$\int_{\mathbf{f}_m} \int_{\mathbf{f}_n} \psi_m(\mathbf{r}) g(\mathbf{r} - \mathbf{r}') \xi_n(\mathbf{r}') d\mathbf{r}' d\mathbf{r} \quad (\text{S.21})$$

where the scalar functions  $\psi_m, \xi_n$  come from the vector basis functions  $\mathbf{f}_m, \mathbf{f}_n$ —they could be the  $x, y$ , or  $z$  component of the vector basis functions, or could be related to the divergence of  $\mathbf{f}_m, \mathbf{f}_n$ .  $g(\mathbf{r} - \mathbf{r}')$  is one of the shift-invariant functions given in Eq. S.17. In the next section, we discuss how we leverage this special form of the matrix elements to accelerate matrix-vector multiplication, which allows for fast iterative solving of the BEM linear system.

## 2.2 Base Approximation Matrices

In this section, we expand on Section 4.1 in the main paper and more thoroughly describe the adaptive integral method (AIM). We also derive the specific forms of the *base approximation* matrices introduced in the paper.

As discussed in our paper, under the AIM formulation, we create a 3D Cartesian grid of point sources surrounding the surface, and replace the scalar functions  $\psi_m, \xi_n$  with linear combinations of Dirac Delta functions localized at nearby grid nodes:

$$\begin{aligned} \psi_m(\mathbf{r}) &\approx \hat{\psi}_m(\mathbf{r}) := \sum_{\mathbf{p} \in S_m} \Lambda_{m\mathbf{p}} \delta^3(\mathbf{r} - \mathbf{p}) \\ \xi_n(\mathbf{r}') &\approx \hat{\xi}_n(\mathbf{r}') := \sum_{\mathbf{q} \in S_n} \Lambda'_{n\mathbf{q}} \delta^3(\mathbf{r}' - \mathbf{q}) \end{aligned} \quad (\text{S.22})$$

Here,  $S_m$  and  $S_n$  are the sets of grid points near each the scalar functions  $\psi_m, \xi_n$ , as illustrated in Fig. 2. The coefficients  $\Lambda_{m\mathbf{p}}, \Lambda'_{n\mathbf{q}}$  are computed based on maximally matching the field radiated by each basis function and that radiated by the corresponding collection of point sources. Specifically, we use the far field matching scheme briefly described in Yang and Yilmaz (2011).

The far field matching scheme requires selecting  $Q$  distinct directions, denoted by  $\hat{\mathbf{r}}_1, \hat{\mathbf{r}}_2, \dots, \hat{\mathbf{r}}_Q$ , a collection of unit vectors. Specifically, we randomly sampled  $Q$  directions that follow a uniform distribution on the upper hemisphere, and use this same collection of directions in all our simulations. To effectively approximate the integral in Eq. S.21, we hope to find a set of coefficients such that

$$\sum_{\mathbf{p} \in S_m} \Lambda_{m\mathbf{p}} g_{\text{far}}(\mathbf{p}, \hat{\mathbf{r}}_i) = \int_{\mathbf{f}_m} \psi_m(\mathbf{r}) g_{\text{far}}(\mathbf{r}, \hat{\mathbf{r}}_i) d\mathbf{r} \quad \text{for } i = 1, 2, \dots, Q \quad (\text{S.23})$$

where  $g_{\text{far}}(\mathbf{p}, \hat{\mathbf{r}}_i) = \lim_{r \rightarrow \infty} g(\mathbf{p} - r\hat{\mathbf{r}}_i)$

The shift-invariant functions given in Eq. S.17, combined with the condition  $kr \gg 1$ , show that Eq. S.23 always reduces to

$$\sum_{\mathbf{p} \in S_m} \Lambda_{m\mathbf{p}} e^{jk\mathbf{p} \cdot \hat{\mathbf{r}}_i} = \int_{\mathbf{f}_m} \psi_m(\mathbf{r}) e^{jk\mathbf{r} \cdot \hat{\mathbf{r}}_i} d\mathbf{r} \quad \text{for } i = 1, 2, \dots, Q \quad (\text{S.24})$$

regardless of the exact form of  $g$  (Eq. S.17 suggests 8 possible forms). Thus, given a collection of unit vectors  $\hat{\mathbf{r}}_1, \hat{\mathbf{r}}_2, \dots, \hat{\mathbf{r}}_Q$ , we can obtain a unique least square system that determines the coefficients  $\Lambda_{m\mathbf{p}}$ .

In practice, we use 48 point sources to approximate each basis function, and use  $Q = 96$ . We find that the condition number of the least square matrix is often large, and we use QR-factorization with column pivoting when solving the least square system.

After determining the coefficients  $\Lambda'_{n\mathbf{q}}$  corresponding to  $\xi_n$  using the same method, we can write

$$\int_{\mathbf{f}_m} \int_{\mathbf{f}_n} \psi_m(\mathbf{r}) g(\mathbf{r} - \mathbf{r}') \xi_n(\mathbf{r}') d\mathbf{r}' d\mathbf{r} \approx \sum_{\mathbf{p} \in S_m} \sum_{\mathbf{q} \in S_n} \Lambda_{m\mathbf{p}} g(\mathbf{p} - \mathbf{q}) \Lambda'_{n\mathbf{q}} \quad (\text{S.25})$$

The approximation above can be written into matrix form, giving rise to the concept of the base approximation ( $B$ ) matrices in the main paper, written as:

$$\begin{aligned} B_{\text{EJ}} &= B_{\text{EJ}}^1 + B_{\text{EJ}}^2; & B_{\text{EM}} &= B_{\text{EM}}^1 + B_{\text{EM}}^2; \\ B_{\text{HJ}} &= B_{\text{HJ}}^1 + B_{\text{HJ}}^2; & B_{\text{HM}} &= B_{\text{HM}}^1 + B_{\text{HM}}^2 \end{aligned} \quad (\text{S.26})$$

where for  $i = 1, 2$

$$\begin{aligned} B_{\text{EJ}}^i &= j\omega\mu_i \cdot (\Lambda_{x,i} G_{1,i} \Lambda_{x,i}^T + \Lambda_{y,i} G_{1,i} \Lambda_{y,i}^T + \Lambda_{z,i} G_{1,i} \Lambda_{z,i}^T) - \frac{j}{\omega\varepsilon_i} \cdot \Lambda_{\nabla,i} G_{1,i} \Lambda_{\nabla,i}^T \\ B_{\text{EM}}^i &= \Lambda_{z,i} G_{2,i} \Lambda_{y,i}^T - \Lambda_{y,i} G_{2,i} \Lambda_{z,i}^T + \Lambda_{x,i} G_{3,i} \Lambda_{z,i}^T - \Lambda_{z,i} G_{3,i} \Lambda_{x,i}^T + \Lambda_{y,i} G_{4,i} \Lambda_{x,i}^T - \Lambda_{x,i} G_{4,i} \Lambda_{y,i}^T \\ B_{\text{HJ}}^i &= \Lambda_{z,i} G_{2,i} \Lambda_{y,i}^T - \Lambda_{y,i} G_{2,i} \Lambda_{z,i}^T + \Lambda_{x,i} G_{3,i} \Lambda_{z,i}^T - \Lambda_{z,i} G_{3,i} \Lambda_{x,i}^T + \Lambda_{y,i} G_{4,i} \Lambda_{x,i}^T - \Lambda_{x,i} G_{4,i} \Lambda_{y,i}^T \\ B_{\text{HM}}^i &= -j\omega\varepsilon_i \cdot (\Lambda_{x,i} G_{1,i} \Lambda_{x,i}^T + \Lambda_{y,i} G_{1,i} \Lambda_{y,i}^T + \Lambda_{z,i} G_{1,i} \Lambda_{z,i}^T) + \frac{j}{\omega\mu_i} \cdot \Lambda_{\nabla,i} G_{1,i} \Lambda_{\nabla,i}^T \end{aligned} \quad (\text{S.27})$$

where the  $\Lambda$  matrices contain approximation coefficients for each basis function, and the  $G$  matrices contain the shift-invariant function values. The  $G$  matrices are thus (three-level) Toeplitz matrices, as noted in [Bleszynski et al. \(1996\)](#). According to Eq. 32–33 in the main paper, multiplying these base matrices to vectors is relatively fast.

## 2.3 Correction Matrices

As stated in our paper, the difference between the exact matrices  $A_X$  and the base approximation matrices  $B_X$  can be considered sparse matrices, since  $B_X^{mn}$  is a good approximation to  $A_X^{mn}$  when the footprints of the basis functions  $\mathbf{f}_m$  and  $\mathbf{f}_n$  are far apart, for  $X \in \{\text{EJ, EM, HJ, HM}\}$ . We exploit this sparseness by defining the correction (C) matrices whose entries are only nonzero if their corresponding basis elements are sufficiently close to each other. The matrix elements are defined as follows:

$$C_X^{mn} = \begin{cases} A_X^{mn} - B_X^{mn} & \text{if } d_{mn} \leq d_{\text{near}} \\ 0 & \text{otherwise} \end{cases} \quad \text{for } X \in \{\text{EJ, EM, HJ, HM}\} \quad (\text{S.28})$$

where  $d_{mn}$  is the distance between the centers of basis functions  $m$  and  $n$  and  $d_{\text{near}}$  is a distance threshold chosen to control the approximation error.

The nonzero elements  $C_X^{mn}$  need to be explicitly computed, by evaluating both  $A_X^{mn}$  from Eq. S.13, S.14, and S.15 and  $B_X^{mn}$  from Eq. S.27. Specifically, using our quadrilateral basis elements, one can easily write an exact matrix element  $A_X^{mn}$  as

$$A_X^{mn} = \int_{\mathbf{f}_m} \int_{\mathbf{f}_n} F(\mathbf{r}, \mathbf{r}') d\mathbf{r} d\mathbf{r}' = \int_{-1}^1 \int_{-1}^1 \int_{-1}^1 \int_{-1}^1 F(u_1, v_1, u_2, v_2) du_1 dv_1 du_2 dv_2 \quad (\text{S.29})$$

since each basis element can be parameterized by two variables  $u, v$ , where  $u, v \in [-1, 1]$  (see Eq. 22–24 in the paper). The exact form of  $F(u_1, v_1, u_2, v_2)$  always contains a term associated with the Green’s function, according to Eq. S.13–S.15. Thus, Eq. S.8 implies that the integrand in Eq. S.29 will contain singularities if overlapping or neighboring basis elements are involved.

### 2.3.1 Overlapping Basis Elements

Having overlapping basis elements essentially means  $(u_1, v_1)$  and  $(u_2, v_2)$  parameterize the same basis element in Eq. S.29. According to Section 3.6 in Gibson (2021), only first-order singularities are associated with overlapping basis elements. To address first-order singularities, we evaluate the integration w.r.t.  $u_1$  and  $v_1$  over  $[-1, 1]$  using a standard Gaussian quadrature, which first approximates Eq. S.29 as

$$A_X^{mn} \approx \sum_{p=1}^M \sum_{q=1}^M w(u_1^p) w(v_1^q) \int_{-1}^1 \int_{-1}^1 F(u_1^p, v_1^q, u_2, v_2) du_2 dv_2 \quad (\text{S.30})$$

The remaining double integral in Eq. S.30 is singular, with a pole of order 1 at  $(u_2, v_2) = (u_1^p, v_1^q)$ , and we remove this singularity by making a change of variables, so that the Jacobian factor will have a zero of order 1 at the same location. Specifically, we first divide the  $[-1, 1]^2$  domain for  $(u_2, v_2)$  into four subdomains according to the position of  $(u_1^p, v_1^q)$ , and then apply change of coordinates in each subdomain.

Fig. 3 illustrates coordinate transformation for one of the four subdomains, where the point  $(u_1^p, v_1^q)$ , which causes a singularity, is mapped to the line segment between  $(0, 1)$  and  $(1, 1)$  in the transformed domain. The resulting Jacobian, when multiplied to the integrand in S.30, effectively removes the singularity. Coordinate transformations can be performed very similarly for the other three subdomains. Following these appropriate coordinate transformations, the double integral can be approximated using Gaussian quadrature, over the new domain.

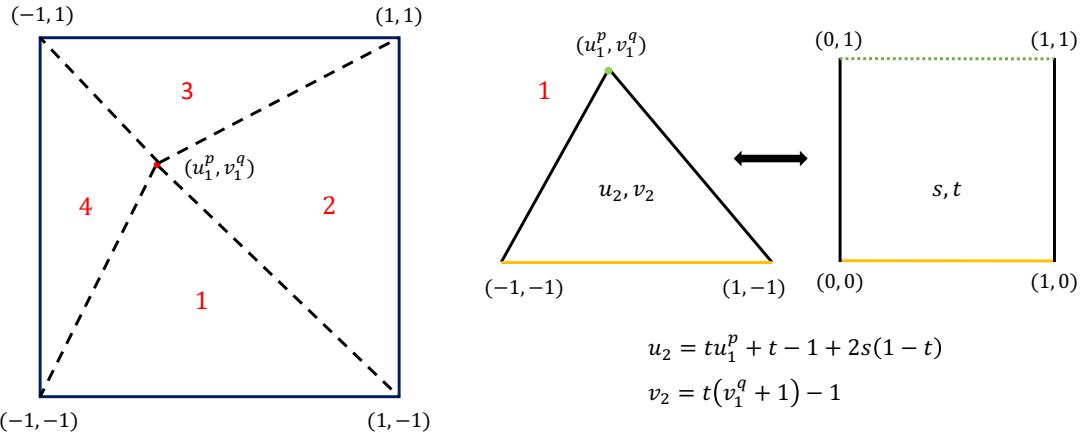


Figure 3: Addressing singularities in matrix elements that involve overlapping basis elements.

### 2.3.2 Neighboring Basis Elements

Neighboring basis elements, which share a common edge, also result in singularities in the integrand in Eq. S.29. According to Section 3.6 in Gibson (2021), depending on the matrix block, which dictates the expression for  $F(u_1, v_1, u_2, v_2)$ , both first-order and second-order singularities need to be addressed. Using horizontally adjacent basis elements as an example, to address high-order singularities, we evaluate the integration using a standard Gaussian quadrature only w.r.t.  $v_1$ , approximating Eq. S.29 as

$$A_X^{mn} \approx \sum_{p=1}^M w(v_1^p) \int_{-1}^1 \int_{-1}^1 \int_{-1}^1 F(u_1, v_1^p, u_2, v_2) du_1 du_2 dv_2 \quad (\text{S.31})$$

while the triple integral needs to be evaluated after applying proper change of coordinates.

Specifically, as shown in Fig. 4, given a fixed value of  $v_1^p$ , our target point  $T_1$  in the left basis element lies on the line segment  $OP$ , while the target point  $T_2$  can be anywhere in the right basis element. A singularity (up to second-order) occurs when both of these target points approach  $P$ . Based on the position of  $P$ , we decompose the basis element on the right into three subdomains, and in each subdomain, we apply a change of coordinates that gives rise to a Jacobian which can cancel out the high-order singularity.

Fig. 4 illustrates an example change of coordinates using one subdomain, showing the mapping between the original parameters  $(u_1, u_2, v_2)$  and the new parameters  $(r, s, t)$  in the transformed domain. Similar 3D coordinate transformations can be applied in the other two subdomains, and the resulting Jacobians cancel out the high-order singularities, allowing for numerical integration in the new domains.

### 2.3.3 Other Matrix Elements

In general, when computing matrix elements that do not involve overlapping or neighboring basis elements, we approximate Eq. S.29 using standard Gaussian quadrature in all the four dimensions:

$$A_X^{mn} \approx \sum_{p=1}^M \sum_{q=1}^M \sum_{r=1}^M \sum_{s=1}^M w(u_1^p) w(v_1^q) w(u_2^r) w(v_2^s) F(u_1^p, v_1^q, u_2^r, v_2^s) \quad (\text{S.32})$$

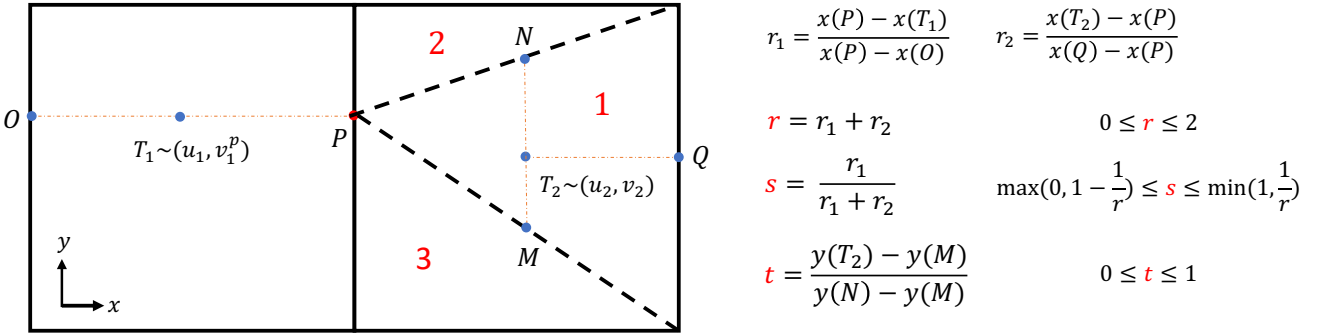


Figure 4: Addressing singularities in matrix elements that involve neighboring basis elements. In the formulas above,  $x, y$  refer to the positions of the points along the respective directions.

### 3 Scattered Field in the Far Field Region

Chapter 3.5 of Gibson (2021) includes detailed derivation of the expressions for the scattered fields generated from surface currents, as computed from the radiation equations. In this section, we list the derived expressions for the scattered fields at an arbitrary point in space, and show how these expressions can be simplified if they are used to evaluate scattered fields in the far field region.

#### 3.1 Scattered Field at an Arbitrary Point

The scattered field values at an arbitrary point in space can be computed from the surface currents, using the source-field relationship in Eq. S.6. In Chapter 3.5 of Gibson (2021), the scattered fields generated by the electric current  $\mathbf{J}$  and magnetic current  $\mathbf{M}$  are expressed separately, and the total scattered field is the sum of the fields radiated by these two types of currents. In the rest of this section, field quantities with subscripts  $A$  are associated with the electric current, and field quantities with subscripts  $F$  are associated with the magnetic current. These notations come from conventions in electromagnetics.

At an arbitrary point  $\mathbf{r}$  in space, the electric field radiated by an electric current  $\mathbf{J}$  is given by:

$$\begin{aligned}
 E_{A,x}(\mathbf{r}) &= -\frac{j}{4\pi\omega\varepsilon} \int_V (C_1 J_x + C_2 [\Delta_x (\Delta_z J_z + \Delta_y J_y) - J_x (\Delta_y^2 + \Delta_z^2)]) d\mathbf{r}' \\
 E_{A,y}(\mathbf{r}) &= -\frac{j}{4\pi\omega\varepsilon} \int_V (C_1 J_y + C_2 [\Delta_y (\Delta_x J_x + \Delta_z J_z) - J_y (\Delta_z^2 + \Delta_x^2)]) d\mathbf{r}' \\
 E_{A,z}(\mathbf{r}) &= -\frac{j}{4\pi\omega\varepsilon} \int_V (C_1 J_z + C_2 [\Delta_z (\Delta_y J_y + \Delta_x J_x) - J_z (\Delta_x^2 + \Delta_y^2)]) d\mathbf{r}' \tag{S.33}
 \end{aligned}$$

where

$$\Delta_x = x - x'; \quad \Delta_y = y - y'; \quad \Delta_z = z - z' \tag{S.34}$$

and  $x, y, z$  and  $x', y', z'$  are the Cartesian components in the vector position  $\mathbf{r}$  and  $\mathbf{r}'$ , respectively ( $\mathbf{r}'$  refers

to points on the radiating surface). The parameters  $C_1, C_2$  are given by

$$\begin{aligned} C_1 &= \frac{2 + 2jkr}{r^3} e^{-jkr} \\ C_2 &= \frac{3 + 3jkr - k^2 r^2}{r^5} e^{-jkr} \end{aligned} \quad (\text{S.35})$$

where  $k$  is the wavenumber of the light and

$$r = |\mathbf{r} - \mathbf{r}'| = \sqrt{(x - x')^2 + (y - y')^2 + (z - z')^2} \quad (\text{S.36})$$

The magnetic field radiated by the electric current  $\mathbf{J}$  is

$$\begin{aligned} H_{A,x}(\mathbf{r}) &= \frac{1}{4\pi} \int_V [\Delta_z J_y - \Delta_y J_z] \frac{1 + jkr}{r^3} e^{-jkr} d\mathbf{r}' \\ H_{A,y}(\mathbf{r}) &= \frac{1}{4\pi} \int_V [\Delta_x J_z - \Delta_z J_x] \frac{1 + jkr}{r^3} e^{-jkr} d\mathbf{r}' \\ H_{A,z}(\mathbf{r}) &= \frac{1}{4\pi} \int_V [\Delta_y J_x - \Delta_x J_y] \frac{1 + jkr}{r^3} e^{-jkr} d\mathbf{r}' \end{aligned} \quad (\text{S.37})$$

Moreover, the electric field radiated by a magnetic current  $\mathbf{M}$  is

$$\begin{aligned} E_{F,x}(\mathbf{r}) &= -\frac{1}{4\pi} \int_V [\Delta_z M_y - \Delta_y M_z] \frac{1 + jkr}{r^3} e^{-jkr} d\mathbf{r}' \\ E_{F,y}(\mathbf{r}) &= -\frac{1}{4\pi} \int_V [\Delta_x M_z - \Delta_z M_x] \frac{1 + jkr}{r^3} e^{-jkr} d\mathbf{r}' \\ E_{F,z}(\mathbf{r}) &= -\frac{1}{4\pi} \int_V [\Delta_y M_x - \Delta_x M_y] \frac{1 + jkr}{r^3} e^{-jkr} d\mathbf{r}' \end{aligned} \quad (\text{S.38})$$

Lastly, the magnetic field radiated by the magnetic current is given by

$$\begin{aligned} H_{F,x}(\mathbf{r}) &= -\frac{j}{4\pi\omega\mu} \int_V (C_1 M_x + C_2 [\Delta_x (\Delta_z M_z + \Delta_y M_y) - M_x (\Delta_y^2 + \Delta_z^2)]) d\mathbf{r}' \\ H_{F,y}(\mathbf{r}) &= -\frac{j}{4\pi\omega\mu} \int_V (C_1 M_y + C_2 [\Delta_y (\Delta_x M_x + \Delta_z M_z) - M_y (\Delta_z^2 + \Delta_x^2)]) d\mathbf{r}' \\ H_{F,z}(\mathbf{r}) &= -\frac{j}{4\pi\omega\mu} \int_V (C_1 M_z + C_2 [\Delta_z (\Delta_y M_y + \Delta_x M_x) - M_z (\Delta_x^2 + \Delta_y^2)]) d\mathbf{r}' \end{aligned} \quad (\text{S.39})$$

where the expressions for  $C_1, C_2$  are the same as in Eq. S.35.

The total scattered fields are given by

$$\mathbf{E}_s(\mathbf{r}) = \mathbf{E}_A(\mathbf{r}) + \mathbf{E}_F(\mathbf{r}); \quad \mathbf{H}_s(\mathbf{r}) = \mathbf{H}_A(\mathbf{r}) + \mathbf{H}_F(\mathbf{r}) \quad (\text{S.40})$$

### 3.2 Far Field Approximations

The expressions in Eq. S.33, S.37, S.38, and S.39 hold for arbitrary points in space. For a point  $\mathbf{r}$  in the far field region, we can write

$$\mathbf{r} = r_0 \hat{\mathbf{r}} = r_0 \langle r_1, r_2, r_3 \rangle \quad (\text{S.41})$$

where we have  $kr_0 \gg 1$  and  $r_1^2 + r_2^2 + r_3^2 = 1$ . We now show that

$$\mathbf{E}_s(\mathbf{r}) \approx \mathbf{E}(\hat{\mathbf{r}}) \frac{e^{-jkr_0}}{r_0}; \quad \mathbf{H}_s(\mathbf{r}) \approx \mathbf{H}(\hat{\mathbf{r}}) \frac{e^{-jkr_0}}{r_0} \quad (\text{S.42})$$

for some quantities  $\mathbf{E}(\hat{\mathbf{r}}), \mathbf{H}(\hat{\mathbf{r}})$  that only depend on the far field scattering direction  $\hat{\mathbf{r}}$ .

We first note that in the far field region, the distance  $r = |r_0\hat{\mathbf{r}} - \mathbf{r}'|$  can be approximated as follows:

$$r = \begin{cases} r_0 - \mathbf{r}' \cdot \hat{\mathbf{r}} & \text{for phase variations} \\ r_0 & \text{for amplitude variations} \end{cases} \quad (\text{S.43})$$

Substituting Eq. S.43 into Eq. S.33 gives us

$$\begin{aligned} E_{A,x}(\mathbf{r}) &= -\frac{j}{4\pi\omega\varepsilon} \int_V (C_1 J_x + C_2 [\Delta_x(\Delta_z J_z + \Delta_y J_y) - J_x(\Delta_y^2 + \Delta_z^2)]) d\mathbf{r}' \\ &= -\frac{j}{4\pi\omega\varepsilon} \frac{2+2jkr_0}{r_0^3} e^{-jkr_0} \int_V J_x e^{jkr' \cdot \hat{\mathbf{r}}} d\mathbf{r}' \\ &- \frac{j}{4\pi\omega\varepsilon} \frac{3+3jkr_0-k^2r_0^2}{r_0^5} e^{-jkr_0} \int_V [\Delta_x(\Delta_z J_z + \Delta_y J_y) - J_x(\Delta_y^2 + \Delta_z^2)] e^{jkr' \cdot \hat{\mathbf{r}}} d\mathbf{r}' \\ &\approx \frac{ke^{-jkr_0}}{2\pi\omega\varepsilon r_0^2} \int_V J_x e^{jkr' \cdot \hat{\mathbf{r}}} d\mathbf{r}' + \frac{jk^2 e^{-jkr_0}}{4\pi\omega\varepsilon r_0^3} \int_V [\Delta_x(\Delta_z J_z + \Delta_y J_y) - J_x(\Delta_y^2 + \Delta_z^2)] e^{jkr' \cdot \hat{\mathbf{r}}} d\mathbf{r}' \quad (\text{S.44}) \\ &\approx \frac{ke^{-jkr_0}}{2\pi\omega\varepsilon r_0^2} \int_V J_x e^{jkr' \cdot \hat{\mathbf{r}}} d\mathbf{r}' + \frac{jk^2 e^{-jkr_0}}{4\pi\omega\varepsilon r_0} \int_V [r_1(r_3 J_z + r_2 J_y) - J_x(r_2^2 + r_3^2)] e^{jkr' \cdot \hat{\mathbf{r}}} d\mathbf{r}' \\ &\approx \frac{jk^2}{4\pi\omega\varepsilon} \frac{e^{-jkr_0}}{r_0} \int_V [r_1(r_3 J_z + r_2 J_y) - J_x(r_2^2 + r_3^2)] e^{jkr' \cdot \hat{\mathbf{r}}} d\mathbf{r}' \\ &= \frac{jk^2}{4\pi\omega\varepsilon} \frac{e^{-jkr_0}}{r_0} [r_1 r_3 \int_V J_z e^{jkr' \cdot \hat{\mathbf{r}}} d\mathbf{r}' + r_1 r_2 \int_V J_y e^{jkr' \cdot \hat{\mathbf{r}}} d\mathbf{r}' - (r_2^2 + r_3^2) \int_V J_x e^{jkr' \cdot \hat{\mathbf{r}}} d\mathbf{r}'] \end{aligned}$$

and similarly

$$\begin{aligned} E_{A,y}(\mathbf{r}) &\approx \frac{jk^2}{4\pi\omega\varepsilon} \frac{e^{-jkr_0}}{r_0} [r_1 r_2 \int_V J_x e^{jkr' \cdot \hat{\mathbf{r}}} d\mathbf{r}' + r_2 r_3 \int_V J_z e^{jkr' \cdot \hat{\mathbf{r}}} d\mathbf{r}' - (r_1^2 + r_3^2) \int_V J_y e^{jkr' \cdot \hat{\mathbf{r}}} d\mathbf{r}'] \\ E_{A,z}(\mathbf{r}) &\approx \frac{jk^2}{4\pi\omega\varepsilon} \frac{e^{-jkr_0}}{r_0} [r_2 r_3 \int_V J_y e^{jkr' \cdot \hat{\mathbf{r}}} d\mathbf{r}' + r_1 r_3 \int_V J_x e^{jkr' \cdot \hat{\mathbf{r}}} d\mathbf{r}' - (r_1^2 + r_2^2) \int_V J_z e^{jkr' \cdot \hat{\mathbf{r}}} d\mathbf{r}'] \quad (\text{S.45}) \end{aligned}$$

Likewise, we also have:

$$H_{F,x}(\mathbf{r}) \approx \frac{jk^2}{4\pi\omega\mu} \frac{e^{-jkr_0}}{r_0} [r_1 r_3 \int_V M_z e^{jkr' \cdot \hat{\mathbf{r}}} d\mathbf{r}' + r_1 r_2 \int_V M_y e^{jkr' \cdot \hat{\mathbf{r}}} d\mathbf{r}' - (r_2^2 + r_3^2) \int_V M_x e^{jkr' \cdot \hat{\mathbf{r}}} d\mathbf{r}'] \quad (\text{S.46})$$

$$H_{F,y}(\mathbf{r}) \approx \frac{jk^2}{4\pi\omega\mu} \frac{e^{-jkr_0}}{r_0} [r_1 r_2 \int_V M_x e^{jkr' \cdot \hat{\mathbf{r}}} d\mathbf{r}' + r_2 r_3 \int_V M_z e^{jkr' \cdot \hat{\mathbf{r}}} d\mathbf{r}' - (r_1^2 + r_3^2) \int_V M_y e^{jkr' \cdot \hat{\mathbf{r}}} d\mathbf{r}'] \quad (\text{S.47})$$

$$H_{F,z}(\mathbf{r}) \approx \frac{jk^2}{4\pi\omega\mu} \frac{e^{-jkr_0}}{r_0} [r_2 r_3 \int_V M_y e^{jkr' \cdot \hat{\mathbf{r}}} d\mathbf{r}' + r_1 r_3 \int_V M_x e^{jkr' \cdot \hat{\mathbf{r}}} d\mathbf{r}' - (r_1^2 + r_2^2) \int_V M_z e^{jkr' \cdot \hat{\mathbf{r}}} d\mathbf{r}'] \quad (\text{S.48})$$

Substituting Eq. S.43 into Eq. S.37 gives us

$$\begin{aligned}
 H_{A,x}(\mathbf{r}) &= \frac{1}{4\pi} \frac{1+jkr_0}{r_0^3} e^{-jkr_0} \int_V [\Delta_z J_y - \Delta_y J_z] e^{jk\mathbf{r}' \cdot \hat{\mathbf{r}}} d\mathbf{r}' \\
 &\approx \frac{jke^{-jkr_0}}{4\pi r_0^2} \int_V [\Delta_z J_y - \Delta_y J_z] e^{jk\mathbf{r}' \cdot \hat{\mathbf{r}}} d\mathbf{r}' \\
 &\approx \frac{jk}{4\pi} \frac{e^{-jkr_0}}{r_0} \int_V [r_3 J_y - r_2 J_z] e^{jk\mathbf{r}' \cdot \hat{\mathbf{r}}} d\mathbf{r}' \\
 &= \frac{jk}{4\pi} \frac{e^{-jkr_0}}{r_0} [r_3 \int_V J_y e^{jk\mathbf{r}' \cdot \hat{\mathbf{r}}} d\mathbf{r}' - r_2 \int_V J_z e^{jk\mathbf{r}' \cdot \hat{\mathbf{r}}} d\mathbf{r}']
 \end{aligned} \tag{S.49}$$

Very similarly, we have:

$$\begin{aligned}
 H_{A,y}(\mathbf{r}) &\approx \frac{jk}{4\pi} \frac{e^{-jkr_0}}{r_0} [r_1 \int_V J_z e^{jk\mathbf{r}' \cdot \hat{\mathbf{r}}} d\mathbf{r}' - r_3 \int_V J_x e^{jk\mathbf{r}' \cdot \hat{\mathbf{r}}} d\mathbf{r}'] \\
 H_{A,z}(\mathbf{r}) &\approx \frac{jk}{4\pi} \frac{e^{-jkr_0}}{r_0} [r_2 \int_V J_x e^{jk\mathbf{r}' \cdot \hat{\mathbf{r}}} d\mathbf{r}' - r_1 \int_V J_y e^{jk\mathbf{r}' \cdot \hat{\mathbf{r}}} d\mathbf{r}']
 \end{aligned} \tag{S.50}$$

Lastly, we also have:

$$E_{F,x}(\mathbf{r}) \approx -\frac{jk}{4\pi} \frac{e^{-jkr_0}}{r_0} [r_3 \int_V M_y e^{jk\mathbf{r}' \cdot \hat{\mathbf{r}}} d\mathbf{r}' - r_2 \int_V M_z e^{jk\mathbf{r}' \cdot \hat{\mathbf{r}}} d\mathbf{r}'] \tag{S.51}$$

$$E_{F,y}(\mathbf{r}) \approx -\frac{jk}{4\pi} \frac{e^{-jkr_0}}{r_0} [r_1 \int_V M_z e^{jk\mathbf{r}' \cdot \hat{\mathbf{r}}} d\mathbf{r}' - r_3 \int_V M_x e^{jk\mathbf{r}' \cdot \hat{\mathbf{r}}} d\mathbf{r}'] \tag{S.52}$$

$$E_{F,z}(\mathbf{r}) \approx -\frac{jk}{4\pi} \frac{e^{-jkr_0}}{r_0} [r_2 \int_V M_x e^{jk\mathbf{r}' \cdot \hat{\mathbf{r}}} d\mathbf{r}' - r_1 \int_V M_y e^{jk\mathbf{r}' \cdot \hat{\mathbf{r}}} d\mathbf{r}'] \tag{S.53}$$

Comparing the above approximations to the scattered field values in the far field region with the claim in Eq. S.42 allows us to write  $\mathbf{E}(\hat{\mathbf{r}})$  and  $\mathbf{H}(\hat{\mathbf{r}})$  in terms of their Cartesian components:

$$\begin{aligned}
 E_x(\hat{\mathbf{r}}) &= -\frac{jk^2}{4\pi\omega\varepsilon} (r_2^2 + r_3^2) F_1(\hat{\mathbf{r}}) + \frac{jk^2}{4\pi\omega\varepsilon} r_1 r_2 F_2(\hat{\mathbf{r}}) + \frac{jk^2}{4\pi\omega\varepsilon} r_1 r_3 F_3(\hat{\mathbf{r}}) - \frac{jk}{4\pi} r_3 F_5(\hat{\mathbf{r}}) + \frac{jk}{4\pi} r_2 F_6(\hat{\mathbf{r}}) \\
 E_y(\hat{\mathbf{r}}) &= \frac{jk^2}{4\pi\omega\varepsilon} r_1 r_2 F_1(\hat{\mathbf{r}}) - \frac{jk^2}{4\pi\omega\varepsilon} (r_1^2 + r_3^2) F_2(\hat{\mathbf{r}}) + \frac{jk^2}{4\pi\omega\varepsilon} r_2 r_3 F_3(\hat{\mathbf{r}}) + \frac{jk}{4\pi} r_3 F_4(\hat{\mathbf{r}}) - \frac{jk}{4\pi} r_1 F_6(\hat{\mathbf{r}}) \\
 E_z(\hat{\mathbf{r}}) &= \frac{jk^2}{4\pi\omega\varepsilon} r_1 r_3 F_1(\hat{\mathbf{r}}) + \frac{jk^2}{4\pi\omega\varepsilon} r_2 r_3 F_2(\hat{\mathbf{r}}) - \frac{jk^2}{4\pi\omega\varepsilon} (r_1^2 + r_2^2) F_3(\hat{\mathbf{r}}) - \frac{jk}{4\pi} r_2 F_4(\hat{\mathbf{r}}) + \frac{jk}{4\pi} r_1 F_5(\hat{\mathbf{r}}) \\
 H_x(\hat{\mathbf{r}}) &= \frac{jk}{4\pi} r_3 F_2(\hat{\mathbf{r}}) - \frac{jk}{4\pi} r_2 F_3(\hat{\mathbf{r}}) - \frac{jk^2}{4\pi\omega\mu} (r_2^2 + r_3^2) F_4(\hat{\mathbf{r}}) + \frac{jk^2}{4\pi\omega\mu} r_1 r_2 F_5(\hat{\mathbf{r}}) + \frac{jk^2}{4\pi\omega\mu} r_1 r_3 F_6(\hat{\mathbf{r}}) \\
 H_y(\hat{\mathbf{r}}) &= -\frac{jk}{4\pi} r_3 F_1(\hat{\mathbf{r}}) + \frac{jk}{4\pi} r_1 F_3(\hat{\mathbf{r}}) + \frac{jk^2}{4\pi\omega\mu} r_1 r_2 F_4(\hat{\mathbf{r}}) - \frac{jk^2}{4\pi\omega\mu} (r_1^2 + r_3^2) F_5(\hat{\mathbf{r}}) + \frac{jk^2}{4\pi\omega\mu} r_2 r_3 F_6(\hat{\mathbf{r}}) \\
 H_z(\hat{\mathbf{r}}) &= \frac{jk}{4\pi} r_2 F_1(\hat{\mathbf{r}}) - \frac{jk}{4\pi} r_1 F_2(\hat{\mathbf{r}}) + \frac{jk^2}{4\pi\omega\mu} r_1 r_3 F_4(\hat{\mathbf{r}}) + \frac{jk^2}{4\pi\omega\mu} r_2 r_3 F_5(\hat{\mathbf{r}}) - \frac{jk^2}{4\pi\omega\mu} (r_1^2 + r_2^2) F_6(\hat{\mathbf{r}})
 \end{aligned} \tag{S.54}$$

where the quantities  $F_1(\hat{\mathbf{r}}), F_2(\hat{\mathbf{r}}), \dots, F_6(\hat{\mathbf{r}})$  are defined as

$$\begin{aligned} F_1(\hat{\mathbf{r}}) &= \int_V J_x(\mathbf{r}') e^{jkr' \cdot \hat{\mathbf{r}}} d\mathbf{r}' \\ F_2(\hat{\mathbf{r}}) &= \int_V J_y(\mathbf{r}') e^{jkr' \cdot \hat{\mathbf{r}}} d\mathbf{r}' \\ F_3(\hat{\mathbf{r}}) &= \int_V J_z(\mathbf{r}') e^{jkr' \cdot \hat{\mathbf{r}}} d\mathbf{r}' \\ F_4(\hat{\mathbf{r}}) &= \int_V M_x(\mathbf{r}') e^{jkr' \cdot \hat{\mathbf{r}}} d\mathbf{r}' \\ F_5(\hat{\mathbf{r}}) &= \int_V M_y(\mathbf{r}') e^{jkr' \cdot \hat{\mathbf{r}}} d\mathbf{r}' \\ F_6(\hat{\mathbf{r}}) &= \int_V M_z(\mathbf{r}') e^{jkr' \cdot \hat{\mathbf{r}}} d\mathbf{r}' \end{aligned} \quad (\text{S.55})$$

### 3.3 Efficient Far Field Scattering Computation

Eq. S.54 shows that  $E_x(\hat{\mathbf{r}})$ ,  $E_y(\hat{\mathbf{r}})$ ,  $E_z(\hat{\mathbf{r}})$ ,  $H_x(\hat{\mathbf{r}})$ ,  $H_y(\hat{\mathbf{r}})$ , and  $H_z(\hat{\mathbf{r}})$  can each be written as a linear combination of the 6 terms in Eq. S.55. Therefore, evaluating the scattered field values in the far field region reduces to efficiently computing  $F_1(\hat{\mathbf{r}}), F_2(\hat{\mathbf{r}}), \dots, F_6(\hat{\mathbf{r}})$ . We use the computation of  $F_1(\hat{\mathbf{r}})$  as an example that shows how the computations can be accelerated using FFT.

Recall that the surface currents are represented using basis functions, and specifically, the  $x$ -directed electric current  $J_x$  can be written as

$$J_x(\mathbf{r}') = \sum_{m=1}^N I_{Jm} \mathbf{f}_{mx}(\mathbf{r}') \quad (\text{S.56})$$

where the coefficients  $I_{Jm}$  are obtained from solving the BEM linear system, and  $\mathbf{f}_{mx}$  refers to the  $x$ -component of the basis functions.

Furthermore, each basis function component  $\mathbf{f}_{mx}$  is approximated using a collection of point sources located in a 3D grid:

$$\mathbf{f}_{mx}(\mathbf{r}') \approx \sum_{\mathbf{p} \in S_m} \Lambda_{m\mathbf{p}} \delta^3(\mathbf{r}' - \mathbf{p}) \quad (\text{S.57})$$

Combining Eq. S.56 and Eq. S.57 shows that

$$J_x(\mathbf{r}') \approx \sum_{\mathbf{p} \in S} \Lambda_{\mathbf{p}} \delta^3(\mathbf{r}' - \mathbf{p}) \quad (\text{S.58})$$

and

$$F_1(\hat{\mathbf{r}}) \approx \sum_{\mathbf{p} \in S} \Lambda_{\mathbf{p}} e^{jk\mathbf{p} \cdot \hat{\mathbf{r}}} \quad (\text{S.59})$$

where  $S$  refers to the collection of all the point sources in the 3D grid. The 3D grid is in fact a regular Cartesian grid, with  $M_x \times M_y \times M_z$  grid points in total, and we denote the spacing between point sources along the  $x, y, z$  directions as  $d_x, d_y, d_z$ . This means we can rewrite Eq. S.59 as

$$F_1(\hat{\mathbf{r}}) \approx \sum_{a=0}^{M_x-1} \sum_{b=0}^{M_y-1} \sum_{c=0}^{M_z-1} \Lambda_{abc} e^{jk(ad_x \cdot r_1 + bd_y \cdot r_2 + cd_z \cdot r_3)} \quad (\text{S.60})$$

Note that we have used the fact that the position of the point source  $\mathbf{p}_{abc}$  can be written as  $(ad_x, bd_y, cd_z)$ . Consider applying the unnormalized inverse discrete Fourier transform to  $\{\Lambda_{abc}\}$ , given by:

$$Y_{uvw} = \sum_{a=0}^{M_x-1} \sum_{b=0}^{M_y-1} \sum_{c=0}^{M_z-1} \Lambda_{abc} e^{2\pi j(au/M_x + bv/M_y + cw/M_z)} \quad (\text{S.61})$$

Comparing Eq. S.60 and Eq. S.61 and incorporating the condition  $k = 2\pi\eta/\lambda$ , we find that applying IFFT on the data grid  $\{\Lambda_{abc}\}$  results in exactly computing  $F_1(\hat{\mathbf{r}})$  for  $\hat{\mathbf{r}} = (r_1, r_2, r_3)$  if we have

$$r_1 = \frac{\lambda u}{M_x d_x \eta}; \quad r_2 = \frac{\lambda v}{M_y d_y \eta}; \quad r_3 = \frac{\lambda w}{M_z d_z \eta} \quad (\text{S.62})$$

for some integers  $(u, v, w)$ . Evaluating  $F_1(\hat{\mathbf{r}})$  for other scattering directions  $\hat{\mathbf{r}}$  relies on interpolation. In practice, we add zero padding to the  $\{\Lambda_{abc}\}$  data grid prior to the IFFT step—thereby increasing  $M_x, M_y, M_z$ —to ensure enough resolution in the frequency domain, so that the trilinear interpolation used for computing  $F_1(\hat{\mathbf{r}})$  can be sufficiently accurate. We find that despite using large data arrays with a lot of zero padding, computing far field scattering using FFT is significantly faster than direction by direction, brute-force evaluation of Eq. S.54.

## 4 Results

In our main paper, we presented simulation results to demonstrate the validity and usefulness of our simulator. This section of the supplemental document presents a larger collection of results, some of which are not included in the paper.

### 4.1 Comparison with Existing Wave Optics Based Reflection Models

Section 6.2 in the main paper presents BRDFs of a few surface samples, computed using five different methods (including our simulation). In this document, we provide some more background on the four first-order methods that we compare our simulation to, and present our full set of surface BRDF plots computed using all the methods.

#### 4.1.1 First-Order Reflection Models

**Scalar Diffraction Models** A recent work by Yan et. al. discusses computing spatial-varying BRDFs with high resolution details, based on scalar diffraction models. We use three of their models for

Model	$\xi_1$	$\xi_2$	$\xi_3$
R-OHS	$\frac{ \psi \cdot \mathbf{n} ^2 F}{4\lambda^2  \omega_i \cdot \mathbf{n}   \omega_o \cdot \mathbf{n} }$	1	2
R-GHS	$\frac{ \psi \cdot \mathbf{n} ^2 F}{4\lambda^2  \omega_i \cdot \mathbf{n}   \omega_o \cdot \mathbf{n} }$	1	$\psi \cdot \mathbf{n}$
Kirchhoff	$\frac{ \psi \cdot \mathbf{n} ^2 F}{4\lambda^2  \omega_i \cdot \mathbf{n}   \omega_o \cdot \mathbf{n} }$	$1 - \frac{\psi \cdot H'(\mathbf{s})}{\psi \cdot \mathbf{n}}$	$\psi \cdot \mathbf{n}$

Table 2: Parameters used in some BRDF models proposed by [Yan et al. \(2018\)](#).  $\mathbf{n}$  is the surface normal on the macro scale and  $F$  is the reflectance of the surface material.  $\omega_i$  and  $\omega_o$  are the incident and outgoing directions of interests, and  $\psi = \omega_i + \omega_o$ .

comparison—the reciprocal original Harvey-Shack (OHS) model, the reciprocal generalized Harvey-Shack (GHS) model, and the Kirchhoff-based model. The BRDFs based on OHS and GHS were derived by approximating the rough surface as a plane that reflects light with a spatially-varying phase shift. The spatially varying phase shifts depend on the surface heights and are approximated using the original Harvey-Shack diffraction theory and the generalized Harvey-Shack theory, which is more accurate for large incident and outgoing angles, as noted in [Krywonos \(2006\)](#). The Kirchhoff-based BRDF is derived from the Kirchhoff diffraction integral, which removes the use of a planar proxy when approximating phase shifts and integrating over the surface.

The readers can refer to [Yan et al. \(2018\)](#) for details on the aforementioned models, and we provide expressions for the derived surface BRDFs. In all the three models, BRDFs can be estimated over individual coherence areas, which are modeled with Gaussian functions. The BRDF values over a coherence area are in the form of

$$f_r(\omega_i, \omega_o) = \frac{\xi_1}{A_c} \left| \int_{\bar{S}_c} w(\mathbf{s} - \mathbf{x}_c) R(\mathbf{s}) e^{-i \frac{2\pi}{\lambda} (\bar{\psi} \cdot \mathbf{s})} d\mathbf{s} \right|^2 \quad (\text{S.63})$$

where  $R(\mathbf{s}) = \xi_2 e^{-i \frac{2\pi}{\lambda} \xi_3 H(\mathbf{s})}$

Here,  $\mathbf{x}_c$  is the center of the coherence area, and  $\bar{S}_c$  is the portion of the target surface within the coherence area, projected onto the xy-plane.  $w(\mathbf{s} - \mathbf{x}_c)$  is a Gaussian function that controls the size of the coherence area, and the normalization factor is given by  $A_c = \int |w(\mathbf{s})| d\mathbf{s}$ . Moreover,  $H(\mathbf{s})$  is the height field function that represents the surface, and the parameters  $\xi_1, \xi_2, \xi_3$  for the three methods are shown in Table 2. Lastly,  $\bar{\psi}$  is the 2D projection of  $\psi$ , which is defined in Table 2.

Therefore, we can easily apply these BRDF models to our surface samples represented by height fields, and for direct comparison, we choose appropriate standard deviations used in the Gaussian function  $w(\mathbf{s} - \mathbf{x}_c)$  to match the Gaussian beam illumination in our simulations.

**Tangent Plane Method** Another first-order reflection model, based on vector rather than scalar fields, is introduced in [Xia et al. \(2023\)](#), and we refer to it as the *tangent plane* method in our work. The tangent plane method is similar to our simulation in that it also involves introducing fictitious current densities on the surface and using these current densities to compute scattered fields from the surface.

However, the tangent plane method is much cheaper than our simulation—the bottleneck in our simulation lies in solving for the surface currents, while the tangent plane method seeks to estimate them. For a point  $\mathbf{r}$  on the surface, the currents  $\mathbf{J}_1(\mathbf{r}), \mathbf{M}_1(\mathbf{r})$  in the exterior region ( $R_1$ ) can be estimated by:

- Evaluate  $\mathbf{E}_i, \mathbf{H}_i$  around  $\mathbf{r}$  and locally approximate the incident field as field from some plane wave
- Construct a plane  $P$  tangent to the surface at the point  $\mathbf{r}$ , using the local surface normal  $\mathbf{n}(\mathbf{r})$
- Estimate the scattered fields  $\mathbf{E}_s(\mathbf{r}), \mathbf{H}_s(\mathbf{r})$  by computing the reflection of the plane wave from  $P$ —closed form formulas can be derived, as noted in e.g. Bohren and Huffman (2008)
- Compute  $\mathbf{J}_1(\mathbf{r}), \mathbf{M}_1(\mathbf{r})$  from Eq. S.3 in Section 1

After approximating the current densities on the entire surface sample, we can apply Eq. S.9 in Section 1 to compute scattering from the surface. Conveniently, when comparing the tangent plane method to our simulations, we can use the exact same incident fields to illuminate the surfaces.

#### 4.1.2 Comparison of BRDFs

We performed simulations on 6 different  $24\mu\text{m} \times 24\mu\text{m}$  surface samples, each discretized into  $960 \times 960$  basis elements. Simulations were done using five incident directions—the normal direction, and four other directions given by  $(\theta_i, \phi_i) = (18^\circ, 0^\circ), (36^\circ, 90^\circ), (54^\circ, 180^\circ), (72^\circ, 270^\circ)$ . The Gaussian beam waists were computed using Eq. 26 in the paper with a primary waist of  $w = 5.5\mu\text{m}$ . The surface material is chosen to be aluminium, and for each incident direction, simulations were performed with 25 wavelengths and 2 linear polarizations. Thus, we perform a total of  $5 \times 25 \times 2 = 250$  simulations for each surface.

The tangent plane method was also applied a total of 250 times for each surface, while the methods from Yan et al. (2018) were each applied 125 times for each surface, since these methods do not distinguish between polarizations. The Gaussian beam incident fields map naturally to the Gaussian coherence kernel used in these methods, allowing us to match the illumination conditions across all methods.

Each BRDF plot in this section is in the form of a hemisphere plot, which visualizes some surface’s BRDF values corresponding to a fixed incident direction and a collection of outgoing directions that cover the upper hemisphere. BRDF values computed from our simulation and the tangent plane method are averaged between two polarizations. The BRDFs are presented in RGB colors, and they are computed using the standard spectral data  $\rightarrow$  XYZ  $\rightarrow$  RGB conversion. Notably, the BRDF values computed from the five different methods match in magnitudes.

Fig. 5–10 contain our full collection of results for each simulated surface. The table in each figure provides a summary of the simulations for all the incident directions on each surface. In the table, the third dimension in the “size” column refers to the range of total height variation in the surface sample. The number of iterations in MINRES solving (using a certain tolerance in the solver code) and the simulation time are similar across wavelengths and polarizations, but vary largely among the surfaces and incident directions. Thus, we provide estimates of these data by averaging across wavelengths and polarizations. Overall, the number of MINRES iterations, and therefore the total simulation time, is larger for incident directions closer to grazing. Simulations on surfaces that are associated with high-order reflection also require more MINRES iterations, as compared to smooth surfaces.

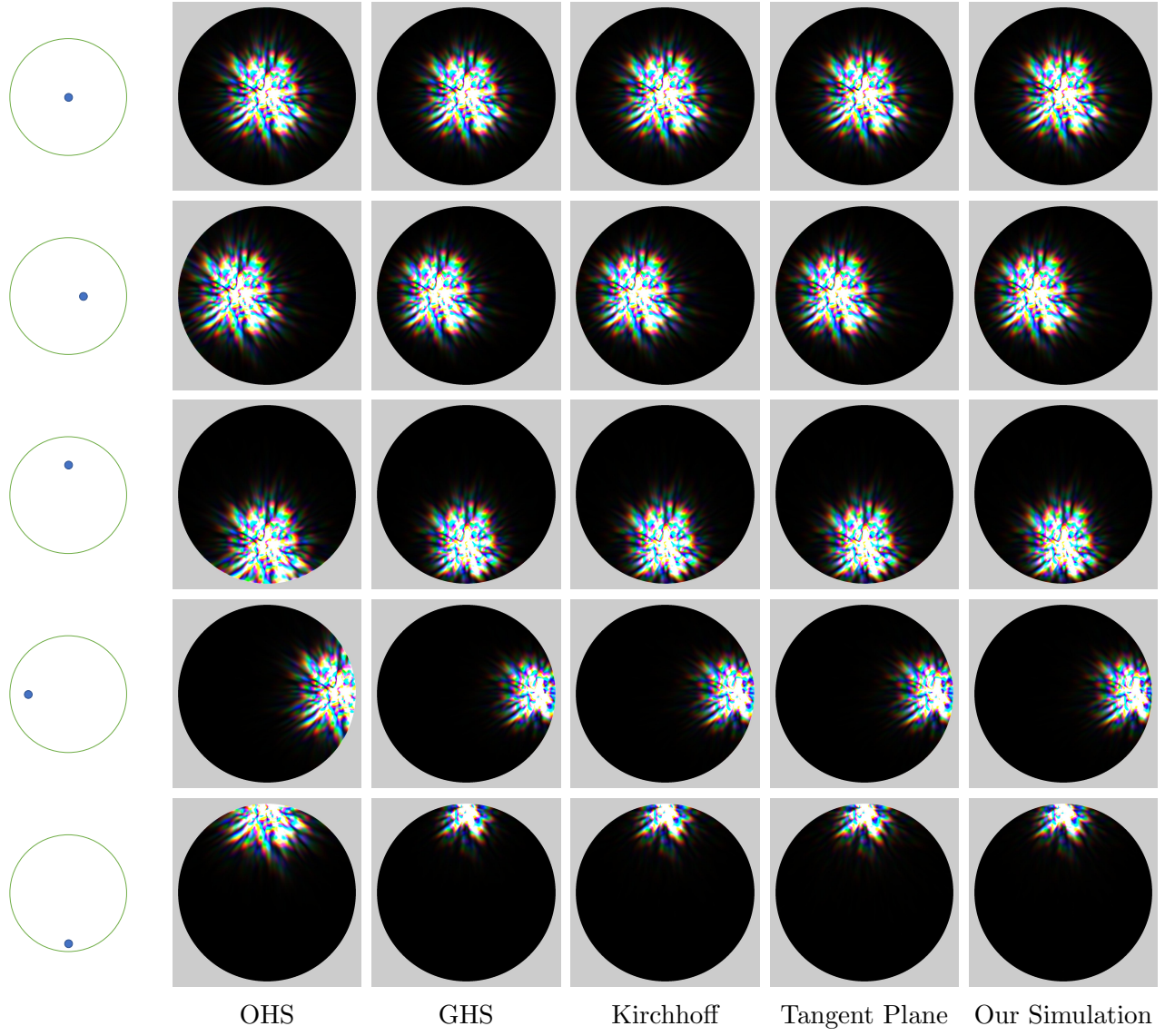
## 4.2 Coherence Areas and BRDFs

In our paper, we demonstrated surface BRDFs corresponding to illumination with different coherence areas. Different coherence areas are represented through combining simulation results from different

subregions on the surface coherently or incoherently. Fig. 13 in the paper shows that for our test surfaces, the BRDFs contain more high resolution details when the illumination is more coherent, and the BRDFs corresponding to less coherent illumination appear blurry. For completeness, in this document we present subregion BRDFs of the two test surfaces, computed from small-area simulations on the surfaces. Fig. 11–14 demonstrate subregion BRDFs (64 per surface), which are relatively smooth because they correspond to small ( $12.5\mu\text{m} \times 12.5\mu\text{m}$ ) areas on the surfaces. The BRDFs for the least coherent illumination shown in Fig. 13 of the main paper are computed from averaging these 64 BRDFs for each surface.

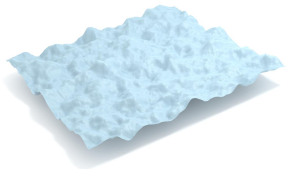
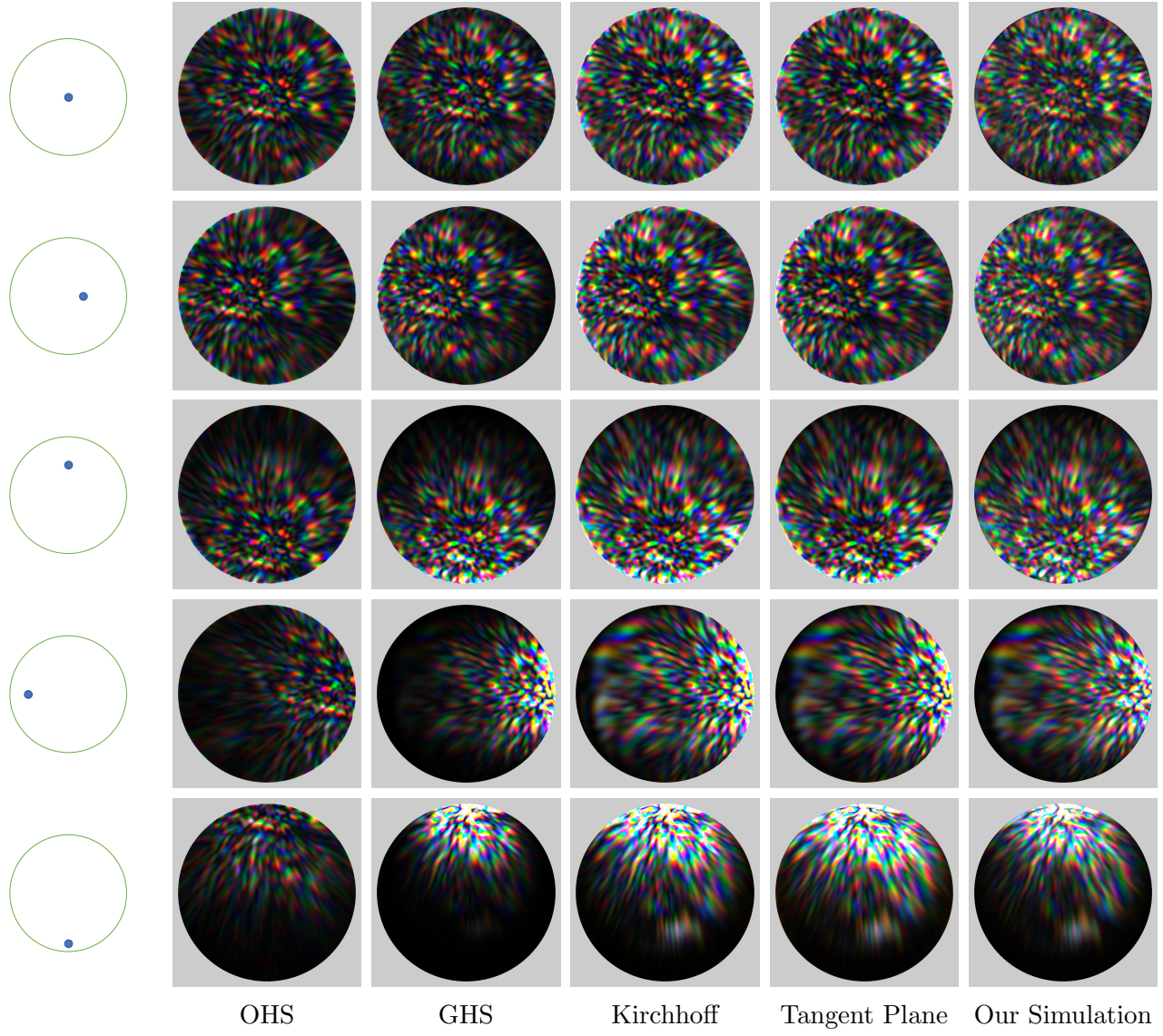
## References

- Elizabeth Bleszynski, Maria Bleszynski, and Thomas Jaroszewicz. 1996. AIM: Adaptive integral method for solving large-scale electromagnetic scattering and radiation problems. *Radio Science* 31, 5 (1996), 1225–1251.
- Craig F Bohren and Donald R Huffman. 2008. *Absorption and scattering of light by small particles*. John Wiley & Sons.
- Walton C Gibson. 2021. *The method of moments in electromagnetics*. CRC press.
- Andrey Krywonos. 2006. *Predicting Surface Scatter using a Linear Systems Formulation of Non-Paraxial Scalar Diffraction*. Ph. D. Dissertation. University of Central Florida.
- Mengqi Xia, Bruce Walter, Christophe Hery, Olivier Maury, Eric Michielssen, and Steve Marschner. 2023. A Practical Wave Optics Reflection Model for Hair and Fur. *ACM Transactions on Graphics (TOG)* 42, 4 (2023).
- Mengqi Xia, Bruce Walter, Eric Michielssen, David Bindel, and Steve Marschner. 2020. A wave optics based fiber scattering model. *ACM Transactions on Graphics (TOG)* 39, 6 (2020), 1–16.
- Lingqi Yan, Milos Hasan, Bruce Walter, Steve Marschner, and Ravi Ramamoorthi. 2018. Rendering Specular Microgeometry with Wave Optics. *ACM Transactions on Graphics*, 37, 4, Article 75 (2018).
- Kai Yang and Ali E Yilmaz. 2011. Comparison of precorrected FFT/adaptive integral method matching schemes. *Microwave and Optical Technology Letters* 53, 6 (2011), 1368–1372.



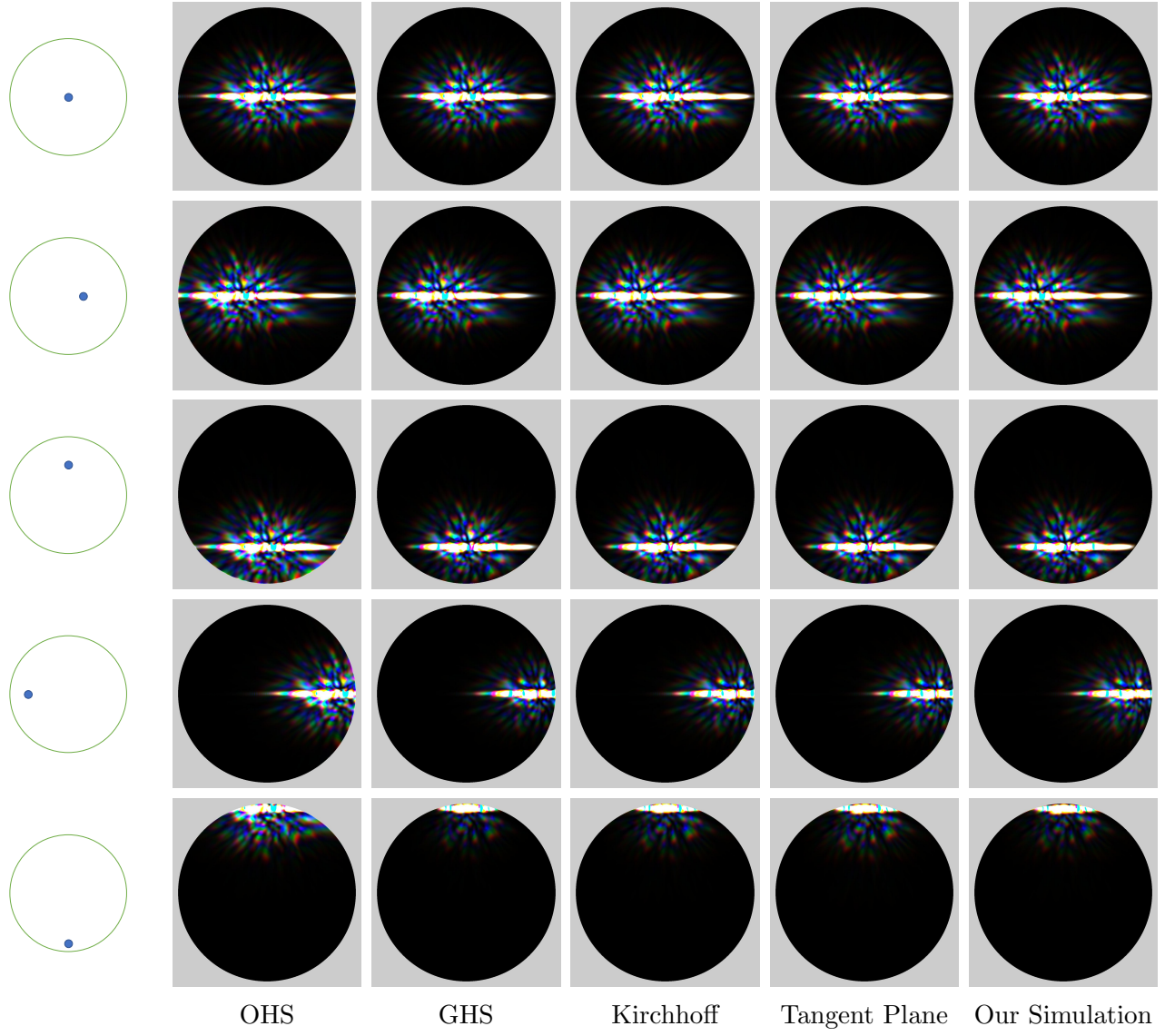
size ( $\mu m$ )	$(\theta_i, \phi_i)$	iterations	time
24 × 24 × 0.6	normal	385	2.8 min
	(18°, 0°)	439	3.0 min
	(36°, 90°)	542	3.5 min
	(54°, 180°)	662	4.2 min
	(72°, 270°)	696	4.4 min

Figure 5: Surface sample 1: low roughness surface with isotropic bumps. The “iterations” entries in the table refer to the number of MINRES iterations used in simulations on this surface illuminated from different incident directions. The “time” entries refer to our total full-wave simulation time corresponding to different incident directions.



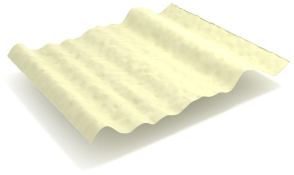
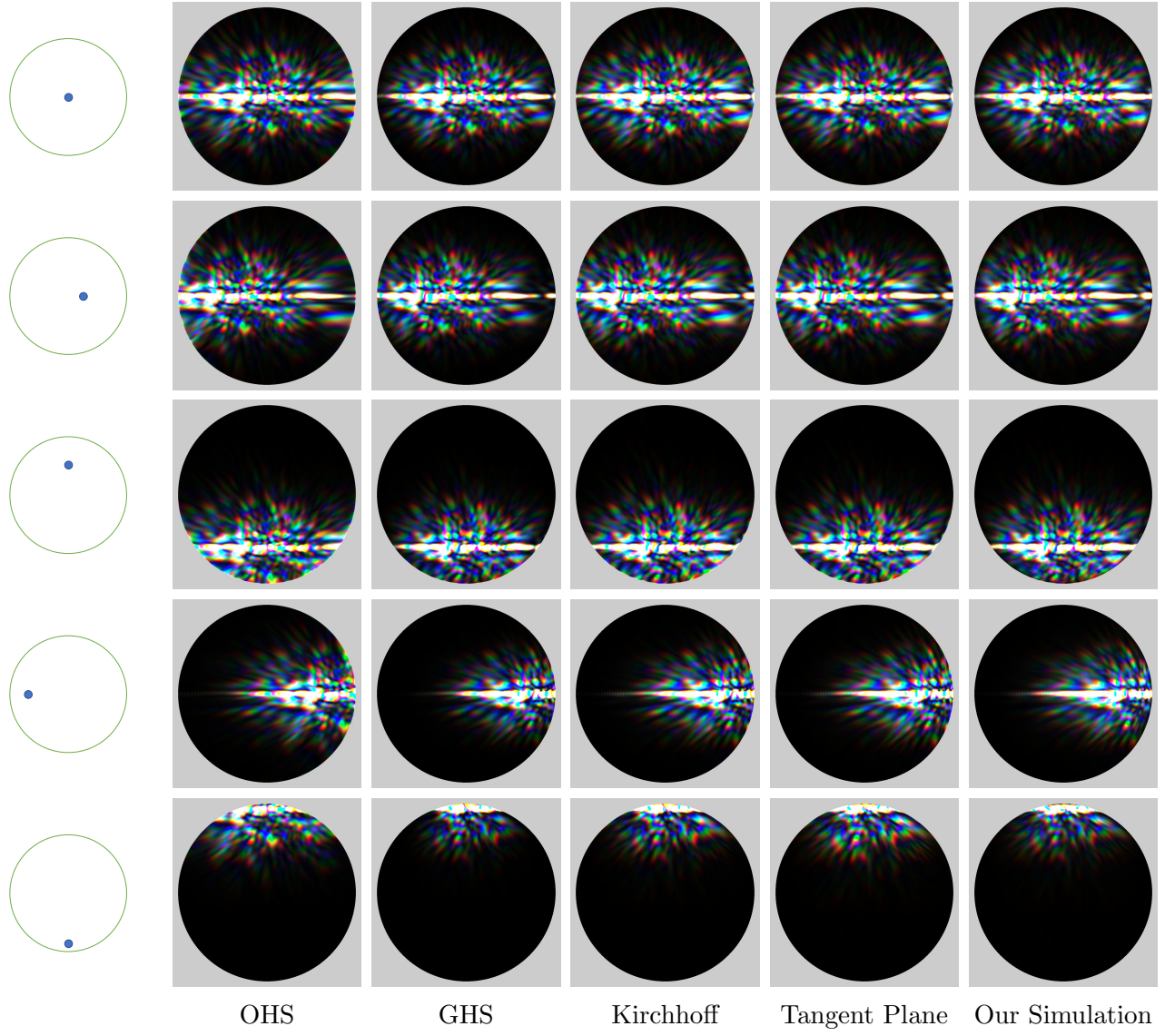
size ( $\mu m$ )	$(\theta_i, \phi_i)$	iterations	time
24 × 24 × 2.7	normal	607	5.3 min
	(18°, 0°)	605	5.2 min
	(36°, 90°)	638	5.5 min
	(54°, 180°)	638	5.5 min
	(72°, 270°)	661	5.7 min

Figure 6: Surface sample 2: high roughness surface with isotropic bumps. The “iterations” entries in the table refer to the number of MINRES iterations used in simulations on this surface illuminated from different incident directions. The “time” entries refer to our total full-wave simulation time corresponding to different incident directions.



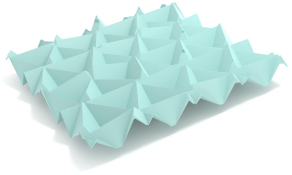
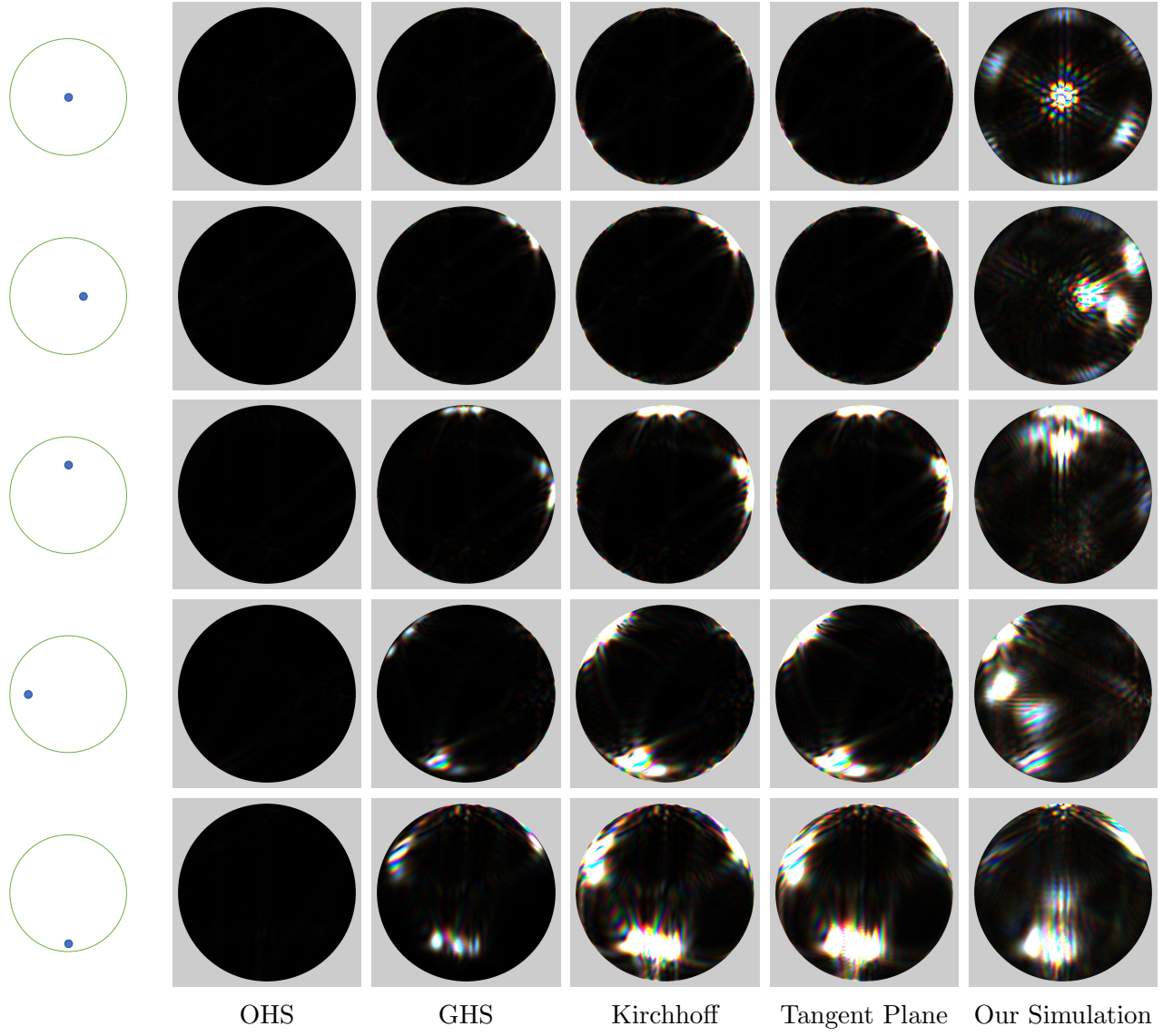
size ( $\mu m$ )	$(\theta_i, \phi_i)$	iterations	time
24 × 24 × 1.3	normal	317	2.6 min
	(18°, 0°)	361	2.8 min
	(36°, 90°)	553	4.0 min
	(54°, 180°)	538	3.9 min
	(72°, 270°)	599	4.3 min

Figure 7: Surface sample 3: low roughness brushed surface. The “iterations” entries in the table refer to the number of MINRES iterations used in simulations on this surface illuminated from different incident directions. The “time” entries refer to our total full-wave simulation time corresponding to different incident directions.



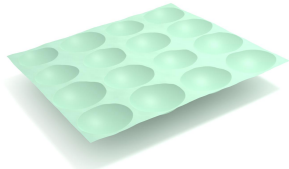
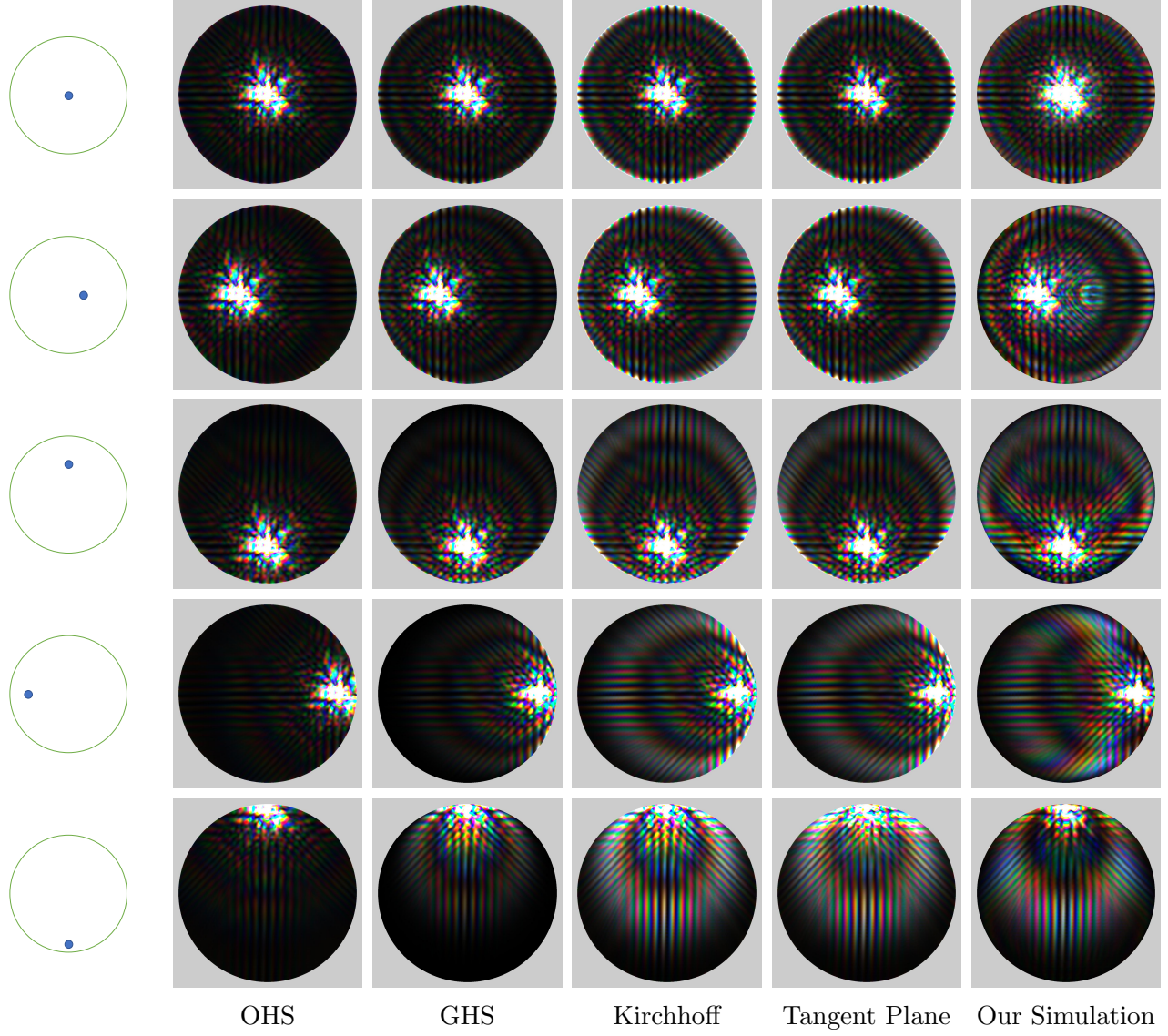
size ( $\mu m$ )	$(\theta_i, \phi_i)$	iterations	time
24 × 24 × 2.6	normal	540	4.9 min
	(18°, 0°)	548	4.9 min
	(36°, 90°)	767	6.6 min
	(54°, 180°)	583	5.2 min
	(72°, 270°)	816	7.0 min

Figure 8: Surface sample 4: high roughness brushed surface. The “iterations” entries in the table refer to the number of MINRES iterations used in simulations on this surface illuminated from different incident directions. The “time” entries refer to our total full-wave simulation time corresponding to different incident directions.



size ( $\mu m$ )	$(\theta_i, \phi_i)$	iterations	time
24 × 24 × 3.9	normal	1468	14.4 min
	(18°, 0°)	1696	16.5 min
	(36°, 90°)	1824	17.7 min
	(54°, 180°)	1782	17.3 min
	(72°, 270°)	1906	18.5 min

Figure 9: Surface sample 5: corner cube reflectors. The “iterations” entries in the table refer to the number of MINRES iterations used in simulations on this surface illuminated from different incident directions. The “time” entries refer to our total full-wave simulation time corresponding to different incident directions.



size ( $\mu m$ )	$(\theta_i, \phi_i)$	iterations	time
24 × 24 × 1.7	normal	644	5.0 min
	(18°, 0°)	651	4.9 min
	(36°, 90°)	681	5.1 min
	(54°, 180°)	770	5.7 min
	(72°, 270°)	816	6.0 min

Figure 10: Surface sample 6: spherical pits. The “iterations” entries in the table refer to the number of MINRES iterations used in simulations on this surface illuminated from different incident directions. The “time” entries refer to our total full-wave simulation time corresponding to different incident directions.

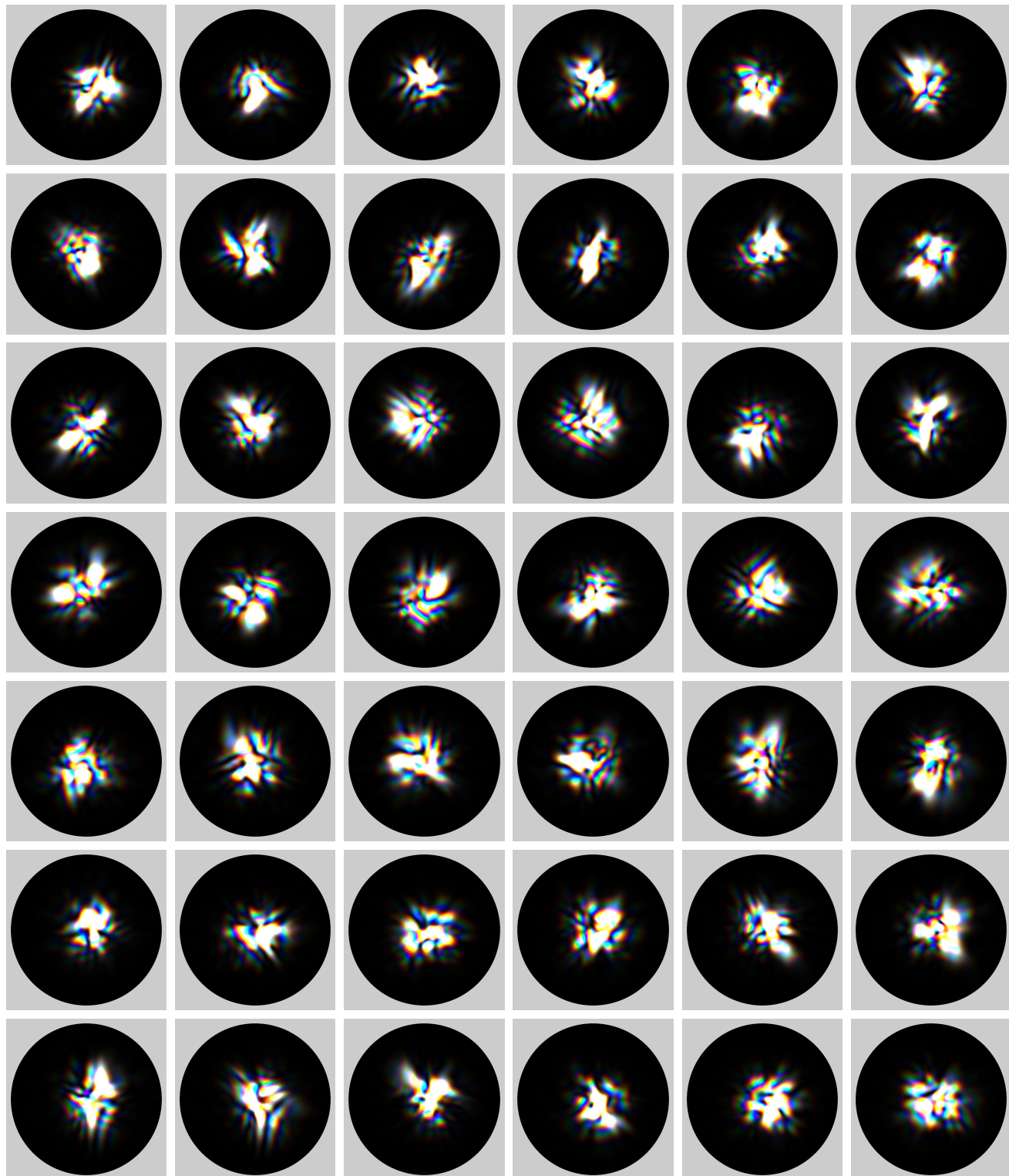


Figure 11: Subregion BRDFs from the bumpy metal surface. See Section 6.3 in our main paper for details on the 64 subregions on the surface.

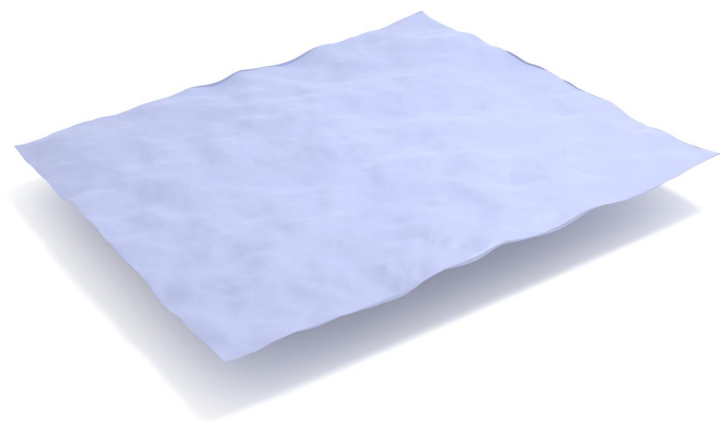
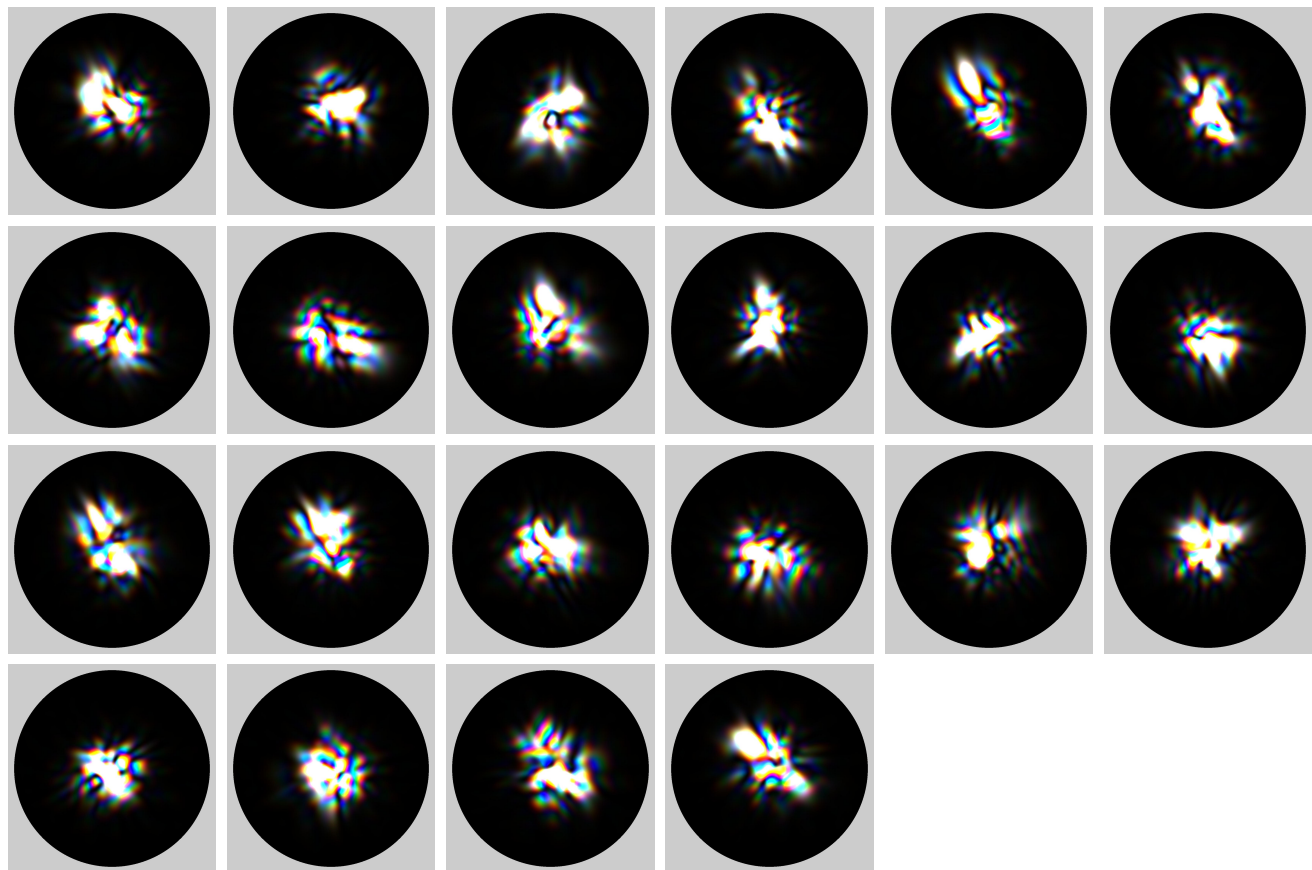


Figure 12: Subregion BRDFs from the bumpy metal surface (continued).

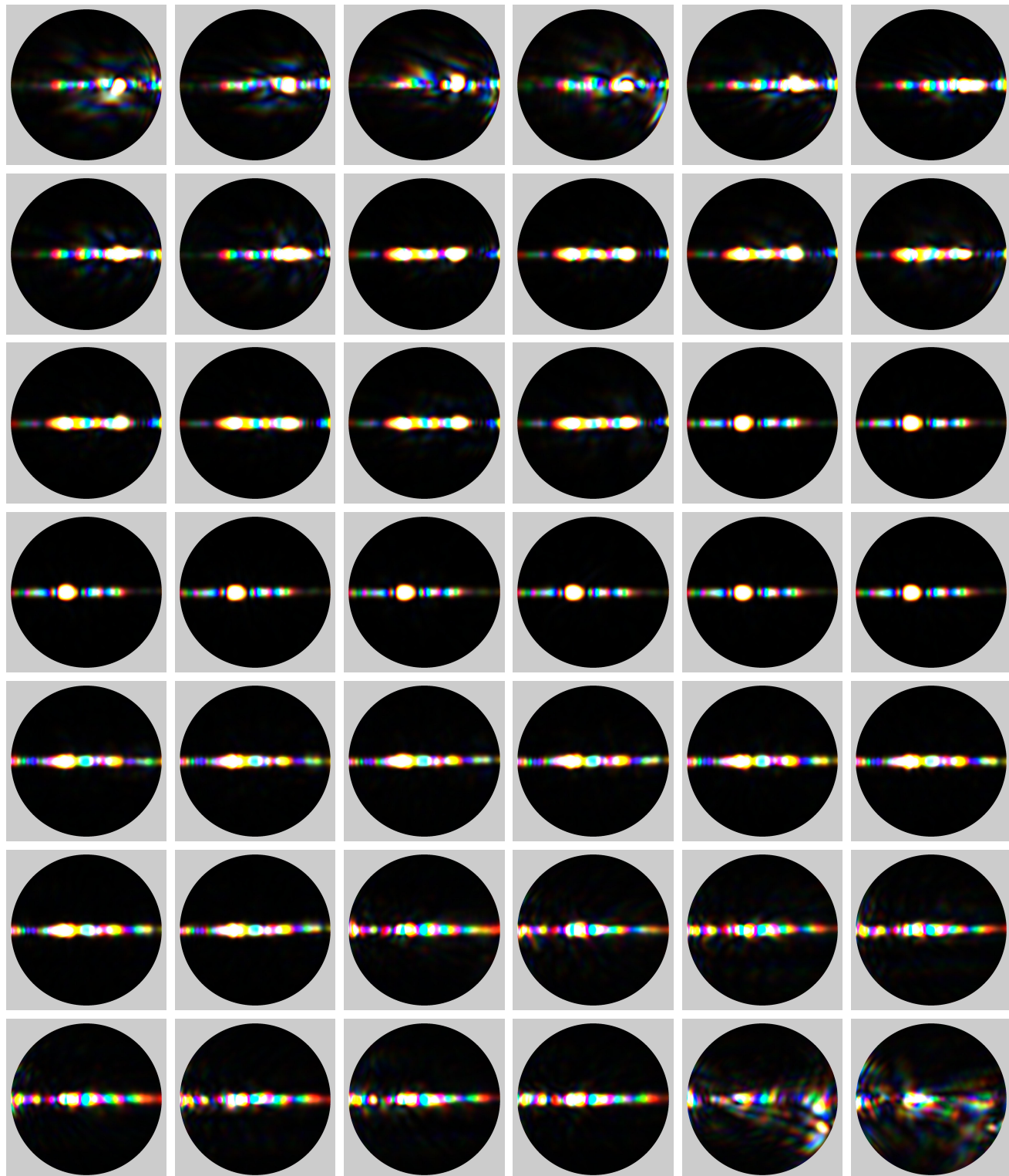


Figure 13: Subregion BRDFs from the brushed metal surface. See Section 6.3 in our main paper for details on the 64 subregions on the surface.

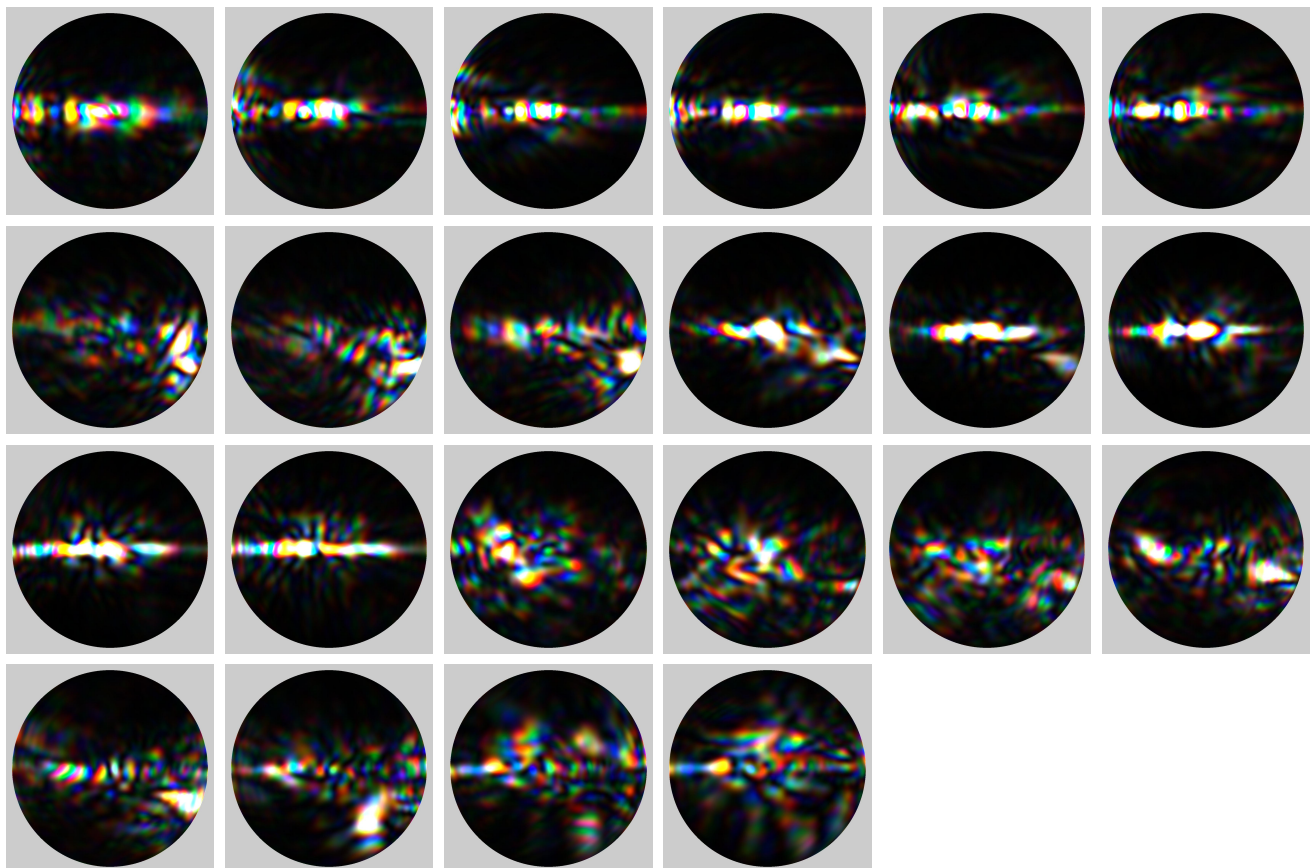


Figure 14: Subregion BRDFs from the brushed metal surface (continued).